



HAL
open science

Assessing the performance of subspace-based modal identification procedures for systems subjected to structural damage and Coulomb-friction non-linearities

P.-É. Charbonnel

► To cite this version:

P.-É. Charbonnel. Assessing the performance of subspace-based modal identification procedures for systems subjected to structural damage and Coulomb-friction non-linearities. *Mechanical Systems and Signal Processing*, 2023, 199, pp.110399. 10.1016/j.ymssp.2023.110399 . cea-04341722

HAL Id: cea-04341722

<https://cea.hal.science/cea-04341722>

Submitted on 14 Mar 2024

HAL is a multi-disciplinary open access archive for the deposit and dissemination of scientific research documents, whether they are published or not. The documents may come from teaching and research institutions in France or abroad, or from public or private research centers.

L'archive ouverte pluridisciplinaire **HAL**, est destinée au dépôt et à la diffusion de documents scientifiques de niveau recherche, publiés ou non, émanant des établissements d'enseignement et de recherche français ou étrangers, des laboratoires publics ou privés.

Assessing the performance of subspace-based modal identification procedures for systems subjected to structural damage and Coulomb-friction non-linearities

P.-É. Charbonnel^a

^a*Université Paris-Saclay, CEA, Service d'Études Mécaniques et Thermiques (SEMT), 91191 Gif-sur-Yvette, France*

Abstract

In this paper, the robustness of subspace-based identification methods for modal analysis is assessed for damaging systems including local Coulomb-friction mechanisms (or equivalently elasto-plasticity). The underlying objective is to capture damage-induced modal feature changes of structures, mainly frequency drop-off and damping increase, knowing that the presence of components with participating friction forces also affects modal signature. The performance of several modal detection procedures is assessed using the data acquired during the JVP (french for ‘Jonction Voile-Plancher’) test campaign during which a reinforced-concrete specimen, anchored to a shaking table by the means of swivels, is submitted to several kind of ground motion inputs of varied level. A comparison between Input/Output versus Output-Only identification is made using both seismic and broad-band random inputs and the potentialities of the modal selection procedures are highlighted for different cases where the two kind of non-linearities (damage occurrence and friction at swivels) are activated in different proportions. Regarding the presence of friction forces when conducting modal analysis, experimental results are backed up by a numerical study that enables a theoretical quantification of the apparent frequency and damping ratio values that should be expected after modal analysis for varied input-to-nonlinear forces ratios.

Keywords:

Operational/Experimental Modal Analysis, Stabilization diagram, Subspace-based system identification, Coulomb-friction forces, Elasto-plastic behavior, Shaking table testing

1. Introduction

Subspace-based modal identification procedures have become a standard for various applications involving structural health monitoring, control-law design or modal analysis [1, 2, 3, 4]. The underlying assumption on which state-space identification and modal description more generally rely is the linearity of the system under study. Classical Structural Health Monitoring (SHM) applications aim at comparing a reference configuration to current configuration [5, 6] with the objective of detecting, localizing or quantifying damage or fault. Structural damage affects the dynamic properties of the monitored structure, inducing changes in the modal parameters (natural frequencies, damping ratios, mode shapes), or in the equivalent eigenstructure representation

Email address: pierreetienne.charbonnel@cea.fr (P.-É. Charbonnel)

of the linear system (eigenvalues and observed eigenvectors). Health diagnosis can thus be done by comparing modal signatures, after modal feature extraction, for local or global damage detection [7, 8, 9, 10, 11, 12, 13], ageing characterization possibly coupled with meteorological effects (temperature, humidity, wind, etc.) [14, 15, 16, 11, 17]. Such kind of modal surveillance involves long-term monitoring and slow modal variations compared to the fundamental natural periods of the healthy structures. Alternatively, faster statistical subspace-based fault detection algorithms can be used for instability detection and alarm triggering [18, 19, 20]; such algorithms aim at detecting changes in the modal signature, without computing it online, but on the basis of fast χ^2 -testing on subspace-based residuals. Such approaches have particularly been used in aeronautics for flutter detection or online damage localization applications when coupled with finite element modeling [21, 22, 23, 24, 25].

Of course, some robustness with respect to non-linearity and possible coupling with different physics of different characteristic times is expected and, hopefully, empirically observed. Let one more particularly mention the study [26] where the capabilities of three Operational Modal Analysis (OMA) procedures based on linear dynamics are compared for identifying the modal behavior of systems with local nonlinear sources of dissipation (damping with quadratic velocity term and static friction). This last study concluded on the robustness of several modal identification algorithms with respect to involved non-linearity. In [27] in turn, a cantilevered glass fiber-reinforced composite beam in a wind tunnel with fluid-structure interaction was successfully identified. This study highlighted that the effect of aeroelastic forces applying on the beam are translated into an increase of damping on the low frequency modes and phase dispersion to be observed on the Mean Phase Deviation (MPD) that gives indication on the modeshape complexity. A discussion and several guidelines are provided for the choice of the modal indicators to retain for defining an automated modal procedure adapted to such case, particularly discarding the MPD as criterion for modal selection. Of course the non-linearity must remain ‘reasonable’ for giving a chance to traditional modal analysis to succeed. In the case of facing stronger non-linearities (impact, geometric non-linearities, etc.), Nonlinear Normal Modes (NNMs) can arise and other approaches dedicated to nonlinear system identification [28, 29, 30, 31], out of the scope of this paper, should be considered, particularly when damage detection is involved (see e.g. [32] among others). From the above cited references, no feedback on subspace-based procedures is provided for systems including solid-friction mechanisms and only OMA techniques are considered; one of the objectives of this paper is to provide this feedback considering both Output-Only (OO) and Input-Output (IO) identification.

The ambition of this paper is to present an attempt of identifying the modal properties of a damaging dynamic system with local non-linearities of Coulomb-friction type, based solely on SubSpace-based State-Space IDentification (4SID) techniques and to illustrate the robustness and limitations of the approach using actual shaking-table tests results and simulated measurements. More precisely, the automated fuzzy-driven modal selection procedure described in [13] will be carried out on accelerometers recordings coming from a Reinforced-Concrete (RC) structure embedded on a shaking table and whose experimental setup includes several rods articulated with swivels where solid friction is expected. Thus, based on this rich experimental dataset obtained under various ground motion inputs (seismic and broad-band random) of different levels, the performance of OO and IO modal identification procedures will be assessed for a complex system faced with two types of non-linearities: structural damage occurrence and friction phenomena at swivels level. Additional details regarding the JVP (french for ‘Jonction Voile-Plancher’ i.e. *wall-slab junction*) test sequence, experimental setup and RC specimen characteristics are given in

[33]; only essential information will be given in the present contribution. The robustness of 4SID procedures has already been experienced in [13] on similar gradually damaging test-sequence on RC structure; in this work, a particular emphasis is put on their performance with respect to Coulomb friction non-linearity. In this perspective, experimental interpretation will be backed up by a numerical study involving a nonlinear single Degree Of Freedom (sDOF) oscillator with solid friction that will enable a heuristic quantification of the modal features that can be theoretically expected after modal analysis for varying input-to-nonlinear forces ratio.

Without anticipating too much, several clues indicate that linear identification has good chances to characterize dynamic systems embedding Coulomb-friction nonlinear mechanisms. Indeed, elastoplastic oscillators (with or without hardening) submitted to random inputs have been the subject of numerous studies since [34]. More recently, in [35], the authors show that, when submitted to a white noise input, the acceleration Pseudo-Spectral Density (PSD) of an elastoplastic oscillator can be very well approximated by a linear equivalent system with increased damping ratio, whereas much more complex frequency content can be empirically observed for systems with stronger kind of non-linearities owing to the presence of NNMs (see e.g. [30] for a discussion on pole combination for systems with quadratic or cubic stiffness and their impact on PSDs). In the present paper, it will be shown that the JVP wall-slab specimen together with its rods and swivel connectors exhibited a clear dominant bending behavior during the test sequence, what can be interpreted as the response of an elastoplastic resonator with hardening, where the permanent residual angular displacement in the swivels plays the role of a plastic strain. Although the range of non-linearity considered in [35] remains small (low ductility demand parameter) compared to what was observed during the JVP campaign with swivels exhibiting locked/unlocked behavior, it could however be expected that a linear equivalent modeling gives a satisfactory description of the dynamics involved. The scrupulous quantification of the Coulomb effects on the modal signature will enable a better interpretation of the damaging process, so that damage occurrence in the RC medium can finally be related to frequency drops and modeshapes changes according to current practice [6].

The paper is then organized as follows. Section 2 gives a summary description of the JVP shaking table test campaign and experimental setup. The gradually damaging test sequence consisting in an alternation of broad-band random excitations and seismic inputs is presented and a special attention is paid to the swivels where the Coulomb friction non-linearities occur. Section 3 gives some recalls on the subspace-based automated modal selection strategy, described in details in [13], and used here as corner-stone for modal identification. Section 4 presents the yielding modal analysis results for the entire JVP test-campaign. The reference modal signature of the experimental system in its initial undamaged configuration is first characterized. Both OO and IO analyses are conducted with the objective of quantifying the coupling between the RC specimen and the shaking-table. Experimental results of the reference configuration are validated by comparison to the Finite Element (FE) model developed and updated in [36]. The modal results obtained after processing the entire JVP database are then presented and potentialities and limitations of the subspace-based IO and OO identification procedures are highlighted for inputs of different nature and varying level. Section 5 proposes a discussion on equivalent linear modeling for systems with nonlinear friction components using a single DOF nonlinear oscillator for describing the dominant low-frequency modal behavior of the experimental specimen. The potentialities of both OO and IO procedures can then be discussed objectively and empirically, based on this numerical study. Section 6 finally gives conclusions.

2. Description of the experimental setup – The JVP test campaign

In October 2018, a vast test campaign took place in the CEA/TAMARIS facility where the $s = 1/4$ reduced-scale RC specimen of FIG. 1 was embedded on the Azalée shaking table for a sequence of damageable seismic ground motions in the x and z directions. The $6 \times 6 \text{ m}^2$ Azalée shaking-table is moved by eight hydraulic actuators of 1000 kN maximum capacity supplied by MTS[©] equipment manufacturer. Four actuators, operating in the (x, y) plane (two actuators per direction), impose the horizontal movement and rotations around z . Four actuators, oriented in the z direction, are anchored below the table for imposing the vertical movement and rotations around x and y . The eight hydraulic jacks are operating in closed loop and the MTS[©] controller enables to reproduce complex seismic loading composed of six independent components (three linear accelerations and three angular accelerations). The complete description of the specimen's geometry and design, acquisition devices and test sequence is available in the reference [33] or internal report [37] (available on demand); only essential information is reported here. On FIG. 1, only the sensors used in the present study are pointed out. For respecting Cauchy-Froude's similitude law [38] (accelerations, strains, stresses and resistance parameters are preserved), the ground motion seismic inputs have been contracted in time of a factor \sqrt{s} and additional masses, in a ratio $(1 - s)/s$ with respect to full scale configuration, must be distributed on the specimen. Let one note that the additional masses clamped on the slabs ($2 \times 940 \text{ kg}$) do not match the requirements imposed by Cauchy-Froude's similitude; the masses have been chosen such as calibrating the value of the first eigenfrequency (bending in the x direction) to reproduce a loading similar to those applied to such systems in operational conditions. In the end, the total mass of the loaded RC specimen (excluding rods and swivels) is approximately 3750 kg.

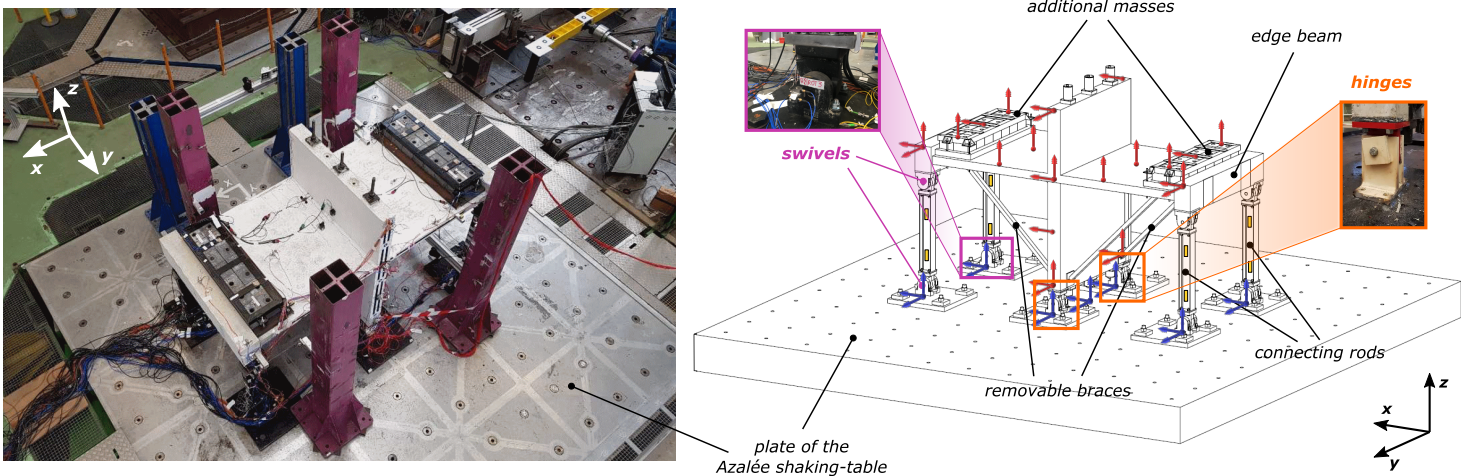


FIGURE 1: View of the reduced-scale RC wall-slab specimen on the $6 \times 6 \text{ m}$ Azalée shaking-table with position of the accelerometers used in this study. Accelerometers on RC the specimen are marked in red, whereas accelerometers on the table are labeled in blue. One arrow is used per measurement direction. Strain gauges on each of the four rods are depicted with yellow rectangles. The oblique steel braces linking the bottom of the wall to the slabs were used for reinforcing the specimen during handling stage and were removed before testing.

The sequencing of the JVP dynamic test campaign is summarized in TAB. 1. The campaign is composed of damaging seismic tests (green lines of the table) where acceleration time-histories are defined as reference input for the controller of the Azalée table in the x and z directions. In terms of Peak Ground Acceleration (PGA), the vertical amplitude is imposed as 60 % of that of the horizontal component. The target acceleration references associated to the other degrees

of freedom of the table (y direction and rotations) are specified to zero, which of course does not mean that no unwanted movement in those directions is possible. After each seismic test, several low-level random tests (white and grey lines of the table) are conducted to quantify the eigenfrequency drop of the specimen after potential damage occurrence. A gaussian white noise is defined as reference input to the MTS[®] controller, such as having the desired Root Mean Square (RMS) acceleration level at the center of the Azalée shaking-table. The signal actually measured on the table is the response of the controlled experimental system to a white noise and verifies ergodicity assumption [39].

TABLE 1: Recap of the JVP test campaign – Dynamic seismic tests along $(x + z)$.

RUN #	Description	Acc. on the table
5	Random broadband input along x	0.006 g RMS
6	Random broadband input along y	0.004 g RMS
7	Random broadband input along z	0.004 g RMS
8	Seismic signal $(x + z)$	PGA _x = 0.18 g PGA _z = 0.15 g
9	Random broadband input along x	0.005 g RMS
10	Random broadband input along y	0.005 g RMS
11	Random broadband input along z	0.004 g RMS
12	Seismic signal $(x + z)$	PGA _x = 0.35 g PGA _z = 0.33 g
13	Random broadband input along x	0.004 g RMS
14	Random broadband input along y	0.006 g RMS
15	Random broadband input along z	0.004 g RMS
16	Seismic signal $(x + z)$	PGA _x = 0.53 g PGA _z = 0.26 g
17	Random broadband input along x	0.004 g RMS
18	Random broadband input along x	0.008 g RMS
19	Random broadband input along y	0.006 g RMS
20	Random broadband input along y	0.013 g RMS
21	Random broadband input along z	0.005 g RMS
22	Random broadband input along z	0.009 g RMS
23	Seismic signal $(x + z)$	PGA _x = 0.71 g PGA _z = 0.48 g
24	Random broadband input along x	0.005 g RMS
25	Random broadband input along x	0.008 g RMS
29*	Random broadband input along y	0.006 g RMS
28	Random broadband input along y	0.014 g RMS
30	Random broadband input along z	0.004 g RMS
31	Random broadband input along z	0.010 g RMS
32	Seismic signal $(x + z)$	PGA _x = 0.89 g PGA _z = 0.58 g
33	Random broadband input along x	0.004 g RMS
34	Random broadband input along x	0.008 g RMS
35	Random broadband input along y	0.004 g RMS
36	Random broadband input along y	0.011 g RMS
37	Random broadband input along z	0.005 g RMS
38	Random broadband input along z	0.011 g RMS
39	Seismic signal $(x + z)$	PGA _x = 1.23 g PGA _z = 0.75 g
40	Random broadband input along x	0.005 g RMS
41	Random broadband input along x	0.008 g RMS
42	Random broadband input along y	0.004 g RMS
43	Random broadband input along y	0.013 g RMS
44	Random broadband input along z	0.005 g RMS
45	Random broadband input along z	0.009 g RMS
46	Seismic signal $(x + z)$	PGA _x = 1.34 g PGA _z = 0.83 g
47	Random broadband input along x	0.006 g RMS
48	Random broadband input along x	0.008 g RMS
49	Random broadband input along y	0.004 g RMS
50	Random broadband input along y	0.012 g RMS
51	Random broadband input along z	0.004 g RMS
52	Random broadband input along z	0.010 g RMS
53	Seismic signal $(x + z)$	PGA _x = 1.60 g PGA _z = 1.02 g

RUN #	Description	Acc. on the table
54	Random broadband input along x	0.005 g RMS
55	Random broadband input along x	0.008 g RMS
56	Random broadband input along y	0.005 g RMS
57	Random broadband input along y	0.013 g RMS
58	Random broadband input along z	0.005 g RMS
59	Random broadband input along z	0.009 g RMS
60	Seismic signal ($x + z$)	PGA $_x$ = 2.06 g PGA $_z$ = 1.21 g
61	Random broadband input along x	0.004 g RMS
62	Random broadband input along x	0.010 g RMS
63	Random broadband input along y	0.005 g RMS
64	Random broadband input along y	0.012 g RMS
65	Random broadband input along z	0.005 g RMS
66	Random broadband input along z	0.010 g RMS

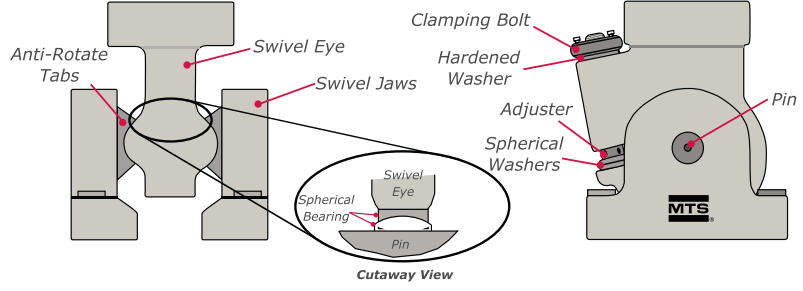
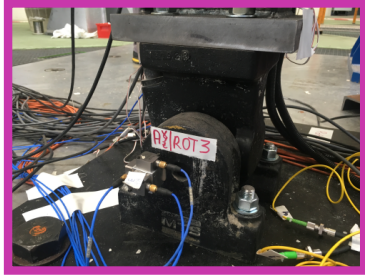
TABLE 1 – Recap of the JVP test campaign – Dynamic seismic tests along ($x + z$).

Regarding RMS values, only acceleration level in the principal loading direction is reported on the table. (*) The inversion concerning RUNs 28 and 29 is deliberate: it corresponds to an actual inversion in the tests recording.

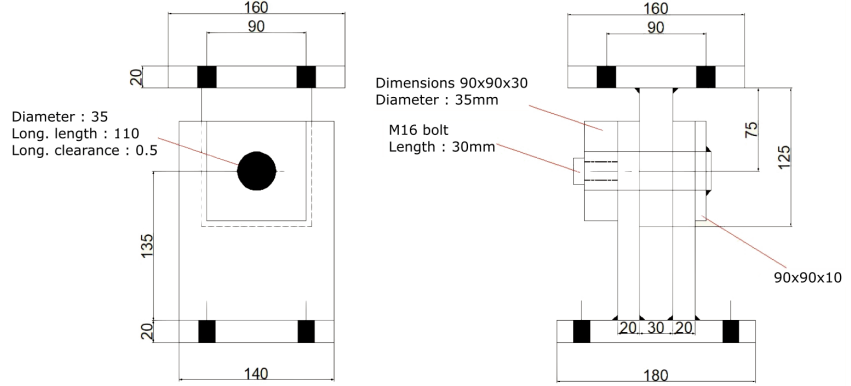
As can be observed on FIG. 1 the boundary conditions for interfacing the RC specimen on the Azalée shaking-table are complex and involve two kind of devices:

- Eight Series 249 MTS swivels (see FIGS 1 and 2a). Two swivels are used at the ends of each vertical rods for ensuring connection between table and specimen. On each swivel, the bi-lateral contact between eye and jaw is maintained using a clamping bolt that applies a pre-stress force transmitted to the spherical bearings surfaces. Although those surfaces are made of Teflon (with very good tribological properties), inevitable friction forces oppose to the relative eye/jaw movement which is translated into a resisting torque at the swivels level. The nonlinear behavior of the swivels have been characterized at LMPS (former LMT Paris-Saclay laboratory) where several quasi-static tests have been performed for characterizing the nonlinear behavior of the swivels. For each joint, the initial tangent stiffness has been identified to $1 \times 10^5 \pm 6 \times 10^4 \text{ N}\cdot\text{m}\cdot\text{rad}^{-1}$ whereas the torque threshold has been estimated as $110 \pm 50 \text{ N}\cdot\text{m}$ (see e.g. [37, sec. 4] or [40, sec. 2.2.4]). Those values, identified in quasistatics, exhibit large dispersion and have to be taken with care in dynamics: no likely angular velocity effect has particularly been characterized.
- Two custom-made hinges (see FIGS 1 and 2b). This assembly has been designed and realized in the CEA/TAMARIS laboratory. The bearing is made of a $\varnothing 35 \text{ mm}$ cylinder with (welded and M16 bolt assembled) end-plates as longitudinal stops, with max. radial clearance of 1 mm for allowing the rotation of the base of the wall with respect to the base. The base is bolted to the Azalée shaking table.

Preliminary investigations, gathered in [36], highlighted the importance of the swivels apparent stiffness on a similar test configuration when processing dynamic hammer shock tests-results. In this last reference indeed, a linear FE model of a cantilevered JVP specimen (different mock-up but identical in design) was derived and the initial tangent stiffness of the swivels was updated by minimization of a modified Constitutive Relation Error (mCRE) functional. The updated stiffness values of the swivels have been computed as $k_y = 1 \times 10^7 \text{ N}\cdot\text{m}$ in the y direction and $k_{\theta_y} = 1.76 \times 10^7 \text{ N}\cdot\text{m}\cdot\text{rad}^{-1}$ around y axis. Of course, those values are associated to the RC finite element model derived in the latter study. However, the updated FE model is able to correctly reproduce, not only the three first eigenmodes as highlighted in the reference, but also most higher frequency modes as the results gathered in forthcoming TAB. 3 can testify.



(a) Series 249 MTS[©] swivels (extracted from MTS[©] documentation).



(b) Custom hinges designed and realized at CEA/TAMARIS (dimensions in mm).

FIGURE 2: Details on the components realizing the boundary conditions with the Azalée shaking-table.

During the 2018-JVP test campaign processed in this paper, a nonlinear behavior, due to frictional contact between the spherical surfaces of the swivels interfacing the vertical rods to the RC specimen and table (see FIG. 1), has been evidenced when processing RUN #5 to #15 test results. Indeed, swivels behave as ‘locked’ at low level and as ‘unlocked’ when excitation level exceeds a certain threshold according to classical Coulomb friction. As an attempt to quantify this phenomenon, two kind of random tests have been realized: (i) *low level random tests* (white lines of the table, expected RMS values: 0.005 g) where swivels are assumed to be locked and (ii) *high level random tests* (grey lines of the table, expected RMS values: 0.010 g) during which a relative movement is expected together with associated friction forces acting on the swivels spherical surface.

3. Methodology – Automated subspace-based state-space identification

The time-histories acquired during the test sequence constitute the set of observable outputs $(y_k)_{k=1}^N \in \mathbb{R}^{m \times N}$ of the experimental system \mathfrak{J} . The latter is composed of the RC specimen itself, the shaking table Azalée and its hydraulic actuators operating in closed-loop. This database is processed using 4SID algorithms that consist in fitting state-space models of increasing orders n to the available measurements after data-projection and inspection of the subspace formed by the columns of the yielding observability matrix. The discrete state matrix A and output matrix C are retrieved from the row spaces of the observability matrix. The poles and modes of the system \mathfrak{J} are computed from the eigenvalues and eigenvectors of A . Details about subspace algorithms are omitted here for conciseness and the interested reader is referred to [1] for theoretical and implementation details and to [13] for details regarding the several variants that have actually

been implemented at CEA/EMSI laboratory within MATLAB[®] framework.

For an appropriate state-space identification, the model order n must be at least twice the number of observable modes. When processing measurements coming from a real structure, one might not know in advance the number of physical modes n^{ph} to be expected on the frequency range of interest. A current practice then consists in over-specifying the model-order (according to CPU limitations) to make sure that no observable mode is missed by the procedure, but one ends up with a collection of n^{sp} unwanted spurious modes that tend to model measurement noise, eventual non-linearities or colored noise inputs. Identification results are then presented in a frequency vs. model-order plot called stabilization diagram and the physical modes must be selected as ‘stable columns’ in the diagram [41]. However, this modal selection stage, when done manually by the experimenter, can be a time-consuming and sometimes inextricable task, even for an experienced user; at least, the selection will depend on the engineering judgment of the person in charge of interpreting the diagrams. In order to bring more robustness to this delicate selection process, a strategy, based on the work of [42], has been proposed in [13] and is summarized on FIG. 3.

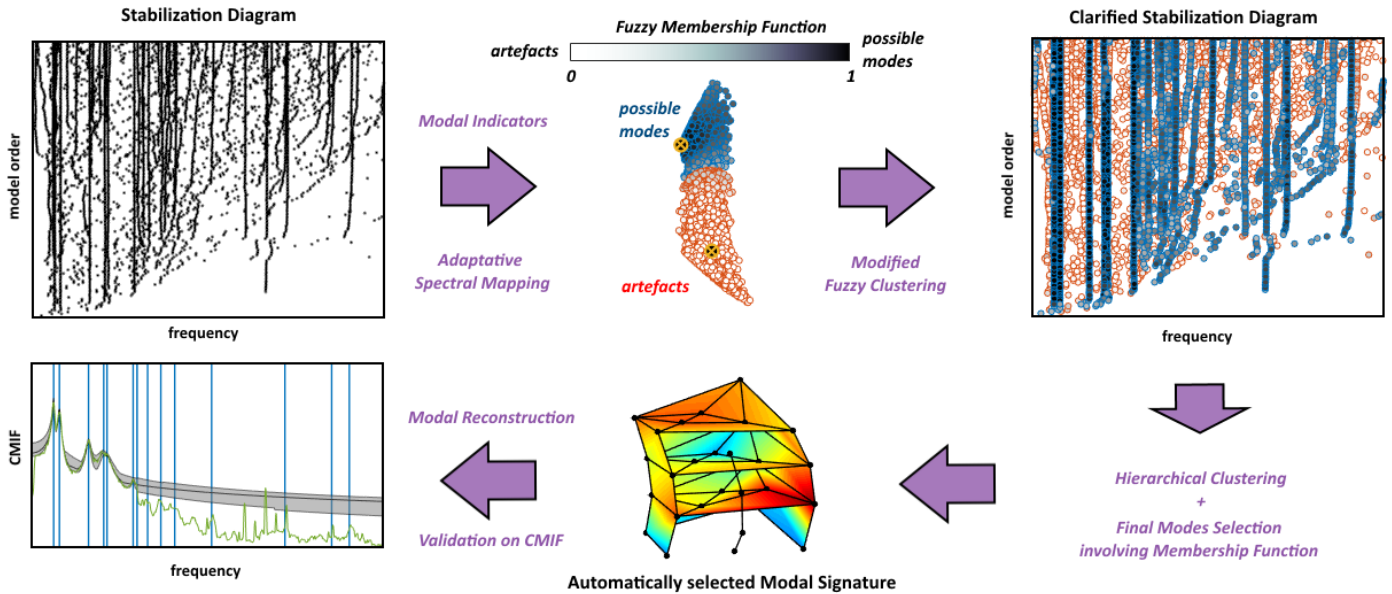


FIGURE 3: Fuzzy-clustering based procedure proposed in [13] for selecting physical modes from highly populated stabilization diagrams.

This strategy consists in three stages:

- stage (i) : eight modal indicators are computed for each mode of the stabilization diagram and a first fuzzy partition is performed in this modal-features space for separating the ‘certainly spurious modes’ from the ‘possibly physical’ candidates. The spurious modes are removed and the membership function resulting from the fuzzy-clustering gives a useful indication on ‘how good’ a physical mode candidate can be;
- stage (ii) : a hierarchical-clustering algorithm is then carried out for building groups of similar modes corresponding to the columns of the stabilization diagram;
- stage (iii) : a final clustering algorithm is used for retaining only the most populated sub-groups identified at stage (ii). Those sub-groups correspond to the physical modes and, after

outlier rejection and polesplitting removal, the most statistically stable member of each sub-group is finally retained for defining the modal signature.

In this study, both Input/Output (IO) and Output-Only (OO) system identification is carried out. OO identification assumes that the dynamic system under study is submitted to unmeasured inputs verifying white-noise assumption. In our case, for intermediate random tests, a multi-axial white-noise reference signal is effectively send to the MTS[®] controller as desired reference acceleration. In this case, the experimental system under study is:

$$\mathfrak{Z}_{OO} = \left\{ \text{RC specimen} + \text{Azalée shaking table} + \text{closed-loop controlled MTS actuators} \right\} \quad (1)$$

Measurements collected in $(y_k)_{k=1}^N$ are considered as outputs of the system \mathfrak{Z}_{OO} and, from an algorithmic point of view, an orthogonal projection of the ‘future outputs’ onto the ‘past outputs’ is realized after forming a block-Hankel matrix containing i block rows. The consistency of subspace methods is proved for $i \rightarrow \infty$ [43]; this number must of course be finite because of memory limitations, however, it should be chosen as large as possible. In this study, the number i of block rows in the block-Hankel matrix has been chosen, as advised by [44], such as verifying:

$$i \geq \frac{f_s}{2f_0} \quad (2)$$

where $f_s = 1/\Delta t$ is the sample frequency and $f_0 \approx 2.5$ Hz is the smallest expected eigenfrequency.

Regarding IO identification, available measurements are split into two groups:

- accelerometers placed on the RC specimen (red arrows of FIG. 1) are considered as outputs and are gathered in $(y_k)_{k=1}^N$;
- accelerometers located on the shaking table (blue arrows of FIG. 1) defining the ground movement imposed to the specimen are considered as inputs and are gathered in $(u_k)_{k=1}^N$.

A block Hankel matrix containing i block rows of input/output data is assembled, but this time, an oblique projection along the subspace formed by the ‘future inputs’ is realized. In this case, the experimental system under study is:

$$\mathfrak{Z}_{IO} = \left\{ \text{RC specimen (cantilevered at Azalée’s plate level)} \right\} \quad (3)$$

This last system also contains the rods, swivels and additional masses and that can be considered as cantilevered at the Azalée’s plate (bottom surface of the swivels).

In this work, the data-driven implementation described in [1] has been used specifying a CVA¹ weighting for OO analysis and combined deterministic-stochastic algorithm with unitary weighting in the IO case. Comparing the results obtained in the OO case and in the IO case, i.e. eigenfrequencies of the system \mathfrak{Z}_{OO} vs. eigenfrequencies of \mathfrak{Z}_{IO} , will give interesting quantification of the coupling between the RC specimen and the shaking device.

¹Canonical Variate Analysis

4. Modal analysis results

4.1. Initial configuration – Experimental characterization after RUN08

The results of the 49 accelerometers placed on the table and specimen according to FIG. 1 have been processed for the RUNs 9, 10 and 11. The 49 time-histories are fed to the subspace identification algorithm for the OO analysis whereas, for the combined IO study, 28 recordings are considered as outputs (sensors in red on FIG. 1) and the 3 accelerations measured at the center of the shaking table are considered as inputs. The number of block rows of the Hankel matrix has been chosen equal to $i = 100$ for respecting the criterion (2). The respective stabilization diagrams obtained after running the 4SID algorithms and automated selection procedure summarized section 3 are presented on FIG. 4. After preliminary examination of the diagrams, one can notice that the mode density is very high but that the modes selected by the automated procedure (in blue) correspond to the peaks of the Complex Mode Indication Function (CMIF) [45] (in green), whose vertical axis is positioned on the right of the diagram. This indicates the overall quality of the modal selection process; the dominant frequency content over the range $[0 ; 100 \text{ Hz}]$ is correctly identified by the fuzzy-automated selection algorithm. An additional comparison with FE modeling (presented later on) will confirm this claim.

One can observe for the OO case that 15 modes have been identified by the procedure. The three first modes dominating the low frequency range $[0 ; 20 \text{ Hz}]$ correspond to the expected bending along x axis (B1x), torsion along z (T1z) and shear-roll along y (R1y) modes. They are followed by two hydraulic modes in the x and y direction respectively denoted (Hx) and (Hy). Indeed, two clear modes coexist around 23 Hz (two modes selected by the subspace-based procedure confirmed by the two peaking singular values on the CMIF); those correspond to a coupling between the oil column stiffness (according to oil's bulk modulus) inside the hydraulic jacks and the inertia of the moving system, *i.e.* Azalée shaking-table and specimen. Those hydraulic modes are associated to the closed loop controlled system and occur for each of the possible moves enabled by the device (three translations and three rotations). Only the lower frequency hydraulic modes associated to x and y translations are clearly observed on the range $[0 ; 100 \text{ Hz}]$. The modal density around 40 Hz is quite high and probably results from a coupling between closely spaced modes due to damping. For such situations one must think about modal subspace rather than nicely decoupled modal response as can be seen for the three first modes. However, the dominant behavior around 40 Hz is driven by the second bending mode (B2x) in the x direction. Let one recall that a currently used criterion for assessing the presence of coupled modes due to damping is [46]:

$$\forall i \neq j, \quad 2\xi_i\omega_i/|\omega_i - \omega_j| \ll 1 \quad (4)$$

If this last criterion is not met (which is the case here), modes i and j are coupled due to damping and form a modal subspace. The same remark can be made around 75 Hz where the third bending mode (B3x) along x is involved on the range $[80 ; 90 \text{ Hz}]$ where several modes interact exhibiting symmetrical and anti-symmetrical slabs and edge beams movements. Modal subspaces are highlighted with colors on the diagrams of FIG. 4 and the modes designation of the structural modes of interest is also added.

For IO analysis in turn, 10 structural modes corresponding to those of the RC specimen \mathfrak{I}_{IO} defined in (3) are identified by the procedure. As expected, one can observe that the oblique projection canceled the influence of the hydraulic modes (Hx) and (Hz) and that higher frequency content is emphasized. The identified modes now correspond to the singular values of the transfer matrix $H(\omega)$ that has been computed from the 28 sensors (in red on FIG. 1) considered as

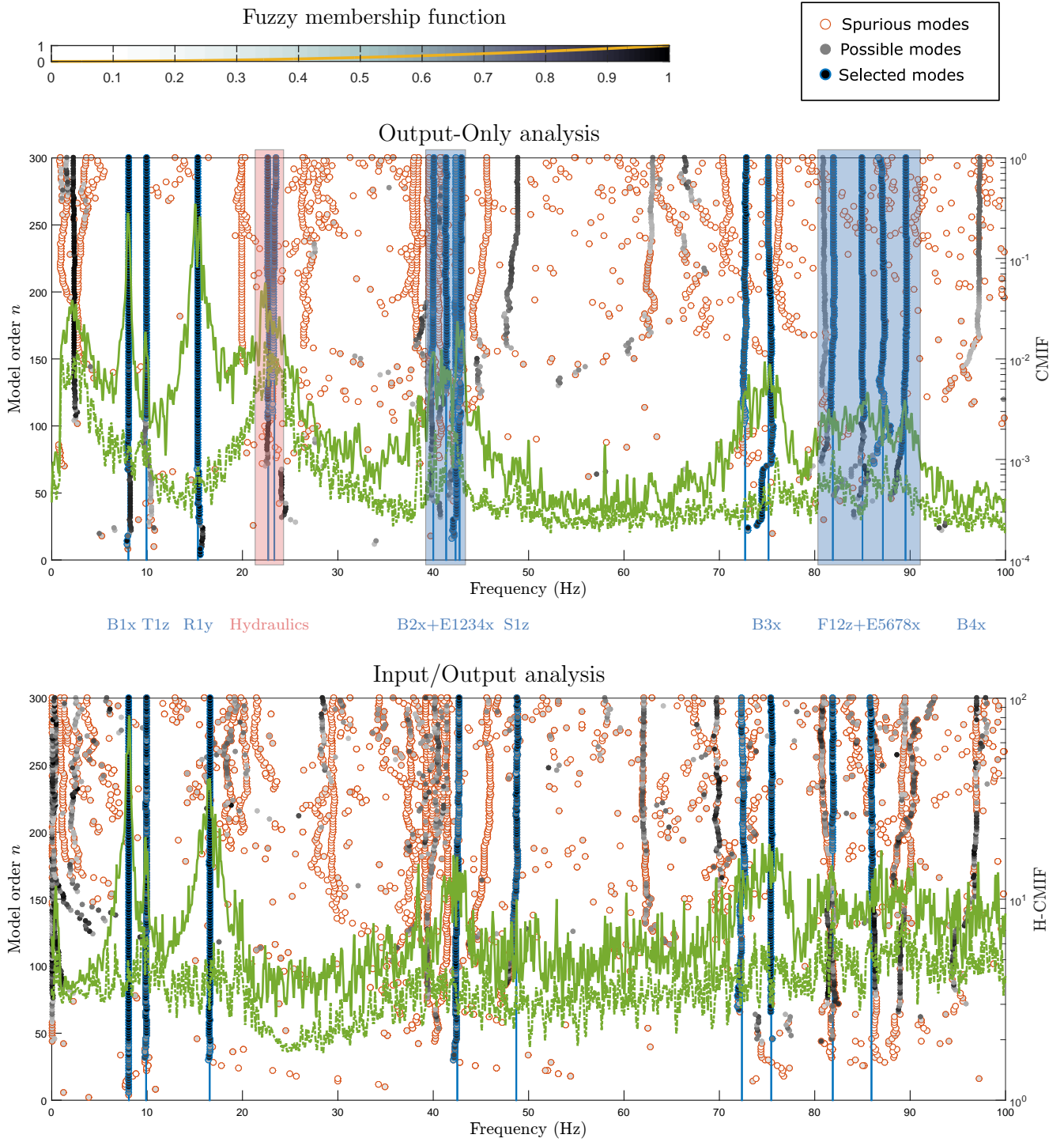


FIGURE 4: Stabilization diagrams obtained when processing data acquired after RUN8. The CMIF values plotted in green in the diagrams correspond to the two first eigenvalues of the PSD matrix for each frequency (OO case), of the transfer matrix H (IO case). Peaks of the CMIF frequency function indicate resonance of the system [45].

outputs and specifying the triaxial acceleration movement of the table as input. The analysis has also been conducted retaining 46 acceleration time-histories as outputs (i.e. the 49 accelerometers on the system minus the 3 table inputs) but no notable difference has been observed on the results; this last study is not reported here. Analogously to the CMIF, the two first singular values of

the transfer matrix $H(\omega)$ are added in green to the plot of FIG. 4 and are labeled as H -CMIF. Once again, the peaks of the H -CMIF are in good accordance with the identified eigenfrequencies which illustrates the relevance of the selected modal signature. One can note the presence of stable columns in the diagrams around 30 Hz and 62 Hz that have not been selected by the procedure. The first one is a residual rotational movement of the specimen and table around the y axis and the second one might be a contribution of the rod modes R*x (see appendix C and TAB. 2, yellow rows) that are barely observable on the selected accelerometers spectral content.

TAB. 2 compares the eigenfrequencies and damping ratios identified for the OO and IO analyses. The same colors, highlighting modal subspaces in the diagrams of FIG. 4, are used in the table for coherence. The eigenfrequencies identified in both cases are very similar, which demonstrates the very low coupling between the RC specimen and the hydraulic shaking device. This observation is not astonishing because the total weight (3.75 tons) of the system $\mathfrak{3}_{\text{IO}}$ embedded on the table is way below the maximum capacity of the eight 100 tons hydraulic actuators applying the dynamic loading. However, one shall note that a slight coupling is observed between the RC specimen and the plate of the Azalée shaking table in the y direction; indeed, the length over which inertia forces (and corresponding momentum) are applied on the table (1.5 m between two swivels) is smaller along the y direction. This yields to an increase of the eigenfrequency value of R1y of nearly 8 % (15.33 to 16.56 Hz).

Mode	Description	OO		IO		FEA	
		freq. [Hz]	damp. [%]	freq. [Hz]	damp. [%]	freq. [Hz]	MAC
B1x	1st bending mode /x	8.04	2.46	8.09	2.05	8.34	0.991
T1z	1st torsion mode /z	9.94	1.68	9.90	1.32	9.52	0.960
R1y	1st shear-roll mode /y	15.33	2.70	16.56	1.56	15.12	0.932
Hx	Hydraulics /x	23.34	6.65				
Hy	Hydraulics /y	22.70	4.87				
E1x	Edge beam bending anti-sym. mode /y + asym. /xy (Snake)	40.00	0.76			37.86	
E2x	Edge beam bending anti-sym. mode /y - sym. /xy (Snake tors.)	41.36	0.92	42.48	1.38	37.86	0.884*
E3x	Edge beam bending sym. mode /y - asym. /xy (Bat)	42.34	0.60			37.86	
E4x	Edge beam bending sym. mode /y - sym. /xy (Bat asym.)	42.76	1.02			37.86	
B2x	2nd bending mode + slabs anti-sym. /z					48.88	
S1z	Slabs symmetric /z			48.71	1.68	49.73	0.912
R1x	Rod bending mode /x					59.52	
R2x	Rod bending mode /x					59.54	
R3x	Rod bending mode /x					59.59	
R4x	Rod bending mode /x	72.70	1.41	72.36	1.33	59.69	0.534*
B3x	3rd bending mode /x (+slabs)	75.15	1.40	75.44	1.26	77.21	0.933
S2z	Slabs symmetric + swivels /z					78.70	
F1z	Slabs antisymmetric + swivels /z (Farfalle asym.)	81.90	1.11	81.89	1.13	82.96	
F2z	Slabs symmetric + swivels /z (Farfalle sym.)	85.00	1.39	85.95	1.30	83.17	0.811*
E5x	Mode E1x + 2nd order bending mode /y	87.15	1.89			114.29	
E6x	Mode E2x + wall torsion /z	89.52	0.88			114.29	
E7x	Mode E3x					114.29	
E8x	Mode E4x					114.29	
B4x	4th bending mode /x (+slabs)			96.80	1.1	116.13	0.376
Ref. to the modeshapes		Appendix A		Appendix B		Appendix C	

TABLE 2: Numerical vs. experimental eigenfrequencies for OO and IO analysis – Initial configuration after RUN08 – The numerical frequencies of the Finite Element Analysis (FEA) have been computed from the model derived by [36]. Classical MAC computation is used for mode-to-mode comparison but is replaced by the (*) cosine of the subspaces-angle when comparing two modal subspaces containing more than one mode (see also the discussion on coupled modes due to damping in the text). Please note that a single color may wrap several modes when modal subspaces are involved. Modeshapes for OO, IO and FE analysis are plotted resp. in appendices A, B and C.

The eigenfrequencies, computed using the FE model borrowed from [36] and derived in within

CAST3M framework, are also added in TAB. 2 for comparison. The model is fully linear and composed of beam- and plate-elements defined in a ‘best estimate’ manner. The swivels are modeled as 6 DOFs stiffness matrices and their stiffness values has been updated using hammershock-tests results by minimizing a modified Constitutive Relation Error (mCRE) functional, as described in the reference. One shall notice the very good adequacy between the model eigenfrequencies and those identified in the OO (and IO) case for the following modes:

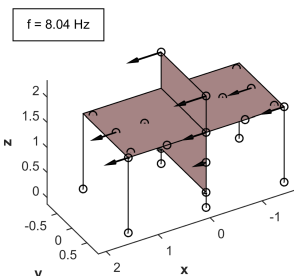
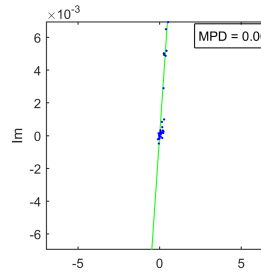
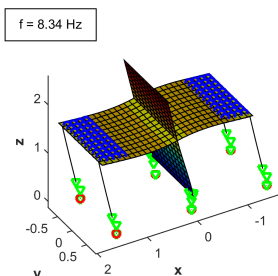
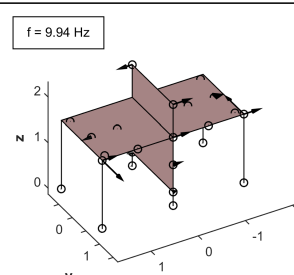
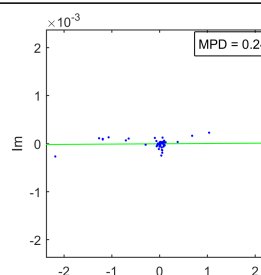
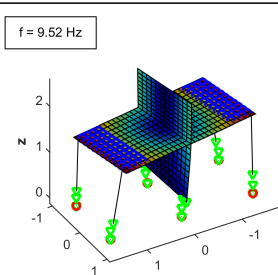
$$L_S = \{B1x, T1z, R1y, B2x, S1z, B3x, F1z+F2z\} \quad (5)$$

with a relative difference of a few percent and Modal Assurance Criterion (MAC) values above 0.8. Note that when considering modal subspaces, the MAC in its classical definition [47] is not suited anymore. However, for such situations, the cosine of the angle between modal subspaces appears as a natural and straightforward generalization of the MAC: this last definition is used in this study when needed.

The other modes of the FE model (rod modes in yellow on TAB. 2) are not found experimentally. The 32 strain-gauges positioned on the four rods (2×4 per rod visible in yellow on FIG. 1) have been processed with the hope of characterizing those modes; unfortunately the observable frequency range $[0; 20 \text{ Hz}]$ enabled by the strain-gauges only led to the identification of the three dominant modes. The strain-gauges analysis is not reported here for conciseness. Let also note that the modes appearing in combination with other modes within modal subspaces cannot be properly plotted.

TAB. 3 compares the experimental and numerical modeshapes computed from the FE model derived by [36]. One can visually and numerically (MAC is recalled) appreciate the very good agreement in terms of eigenfrequencies and modeshapes, which confirms the quality of the modal analysis when processing this first set of test-results. Experimental modeshapes are extracted after OO analysis for the modes in the list L_S except for $S1z$ that has been missed by the algorithm; corresponding modeshape provided by the IO analysis is plotted for this mode.

TABLE 3: Experimental vs. numerical modeshapes – Initial configuration after RUN08.

Mode	Experimental Modeshape	Experimental Colin. Inspection	Numerical Modeshape	MAC
B1x				0.991
T1z				0.960

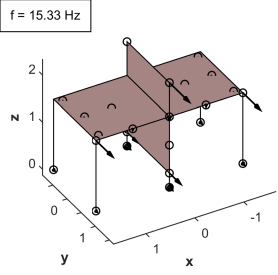
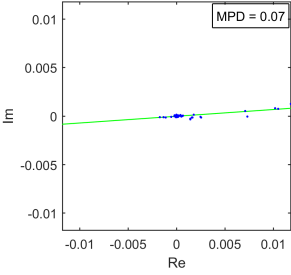
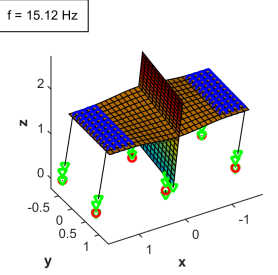
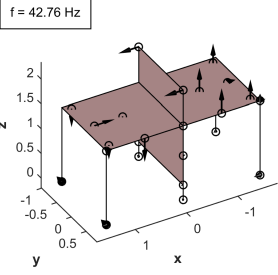
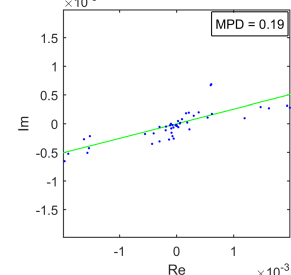
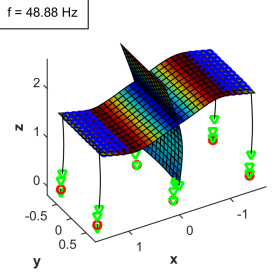
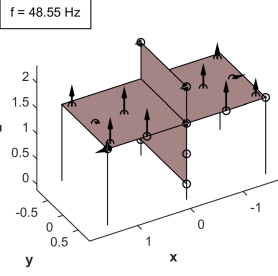
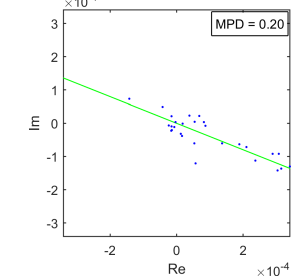
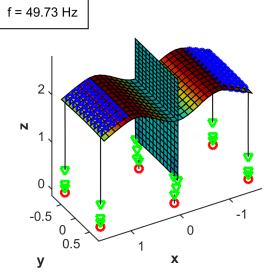
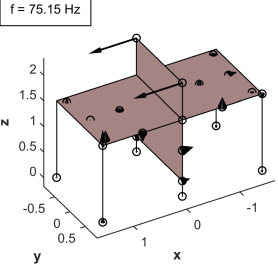
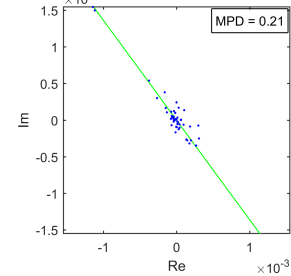
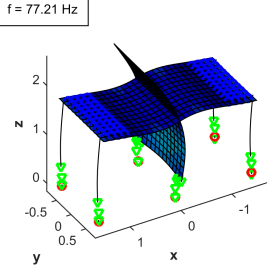
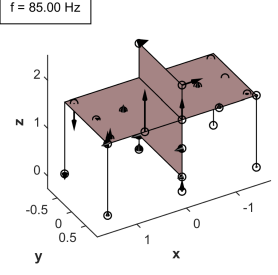
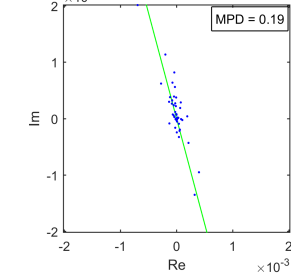
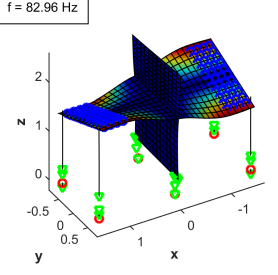
Mode	Experimental Modeshape	Experimental Colin. Inspection	Numerical Modeshape	MAC
R1y				0.932
B2x				0.884*
S1z [◊]				0.912
B3x				0.933
F1z				0.811*

TABLE 3: Experimental vs. numerical modeshapes – Initial configuration after RUN08. Undamped frequency values are recalled next to each modeshape. The colinearity inspection is done by plotting the modeshape in the complex plane and corresponding MPD value is given. A decoupled physical mode will typically be distributed as a straight line in the complex plane, exhibiting a low MPD value. (*) indicates when the classical MAC value is replaced by the cosine of the angle between subspaces. (◊) mode identified in the IO context. On numerical modeshapes, blue circles indicate additional mass, red circles the nodes that have been suppressed for modeling boundary conditions, green triangles extra nodes that have been added to describe the kinematic behavior of the swivels.

The modeshapes associated to the OO, IO and FE analysis are respectively plotted in appendices A, B and C. To end this first subsection of results, one can conclude that the low level tests are clearly dominated by the three first eigenfrequencies and that the FE model updated in [36] was able to correctly predict the modal behavior of the experimental specimen (excluding hydraulics) up to 100 Hz.

4.2. Processing the complete test campaign – Evolution of the modal signature for different analyses

Starting from this reference initial configuration, the capabilities of the modal selection algorithm [13] and more generally subspace-based identification procedures are now assessed in the presence of increasing non-linearities. A particular focus is made on the three first dominant modes.

4.2.1. Broad-band random tests – Evolution of the three first eigenfrequencies

The modal identification algorithms detailed in section 3 are now run for processing the full test campaign. Let one recall that the experimental system identified in the IO case does not include the shaking-table and its hydraulic actuators and corresponds to a cantilevered configuration of the specimen at the shaking table’s plate level (see systems (1) and (3) for comparison). Both low- and high-level intermediate random tests have been processed and the mean values of the three first eigenfrequencies identified along the test-campaign are reported in TAB. 4.

Level	Analysis	After RUN08	After RUN12	After RUN16	After RUN23	After RUN32	After RUN39	After RUN46	After RUN53	After RUN60
LOW	OO	8.04	7.32	6.71	6.50	6.25	6.04	5.83	5.68	5.73
		9.94	9.88	9.88	9.37	9.63	9.42	9.02	8.86	8.65
		15.33	15.31	15.26	14.59	15.16	14.80	14.44	14.08	13.52
	IO	8.09	7.41	6.76	6.46	6.30	5.95	5.76	5.61	5.57
		9.90	9.84	9.73	9.59	9.53	9.37	9.02	8.79	8.52
		16.56	16.42	16.21	16.02	15.81	15.45	14.92	14.76	14.08
HIGH	OO			5.99	6.02 – 6.48	5.95	5.64 – 5.85	4.93 – 5.57	5.59	5.55
				9.55	9.42	9.40	9.20	8.86	8.65	8.39
				15.11	14.72	14.96	14.43	14.17	13.90	13.37
	IO			6.09	5.77	5.51	5.23	5.09	4.96	4.65
				9.42	9.33	9.23	8.85	8.68	8.40	8.04
				16.27	15.99	15.63	15.33	15.03	14.61	13.95

TABLE 4: Three first eigenfrequencies in Hz, identified for low- and high-level random tests.

The RMS accelerations measured on the Azalée table during random tests are reported in TAB. 1. The identification of the first mode B1x was not systematically straightforward when processing high-level tests; corresponding eigenfrequencies are given within intervals in this case. The tracking of mode B1x is the subject of upcoming subsection 4.2.2.

Regarding the identification of linear systems with analogous frequencies, the precision obtained on eigenfrequencies is approximately 0.1 Hz using the methodology described in section 3 and considering the available measurements (≈ 30 s long recordings). A better precision could have been obtained if recordings were of longer duration. Then, a first observation can straightforwardly be made. Eigenfrequency values identified in the OO and IO case are very similar to the precision of the methodology (≈ 0.1 Hz in the present case); only a noticeable decay in frequency of ≈ 1 Hz is visible on the third mode R1y because of the (low) coupling with the shaking table in that direction (see section 4.1).

Now comparing low- and high-level test results, one can observe a clear systematic decay of ≈ 0.7 Hz regarding mode B1x and a smaller decay of ≈ 0.35 Hz regarding mode T1z. This can be

attributed to the nonlinear behavior of the swivels (see FIG. 1) as will be detailed in upcoming subsection 4.2.2 and studied using simple numerical model in section 5. Owing to this non-linearity, the identification of mode B1x was very complicated in the high-level case because more complex frequency content was present around the first eigenfrequency. The automated selection procedure sometimes missed the first mode or flagged it as ‘artefact’ because of higher damping values and generally less stable modal properties. For this reason, eigenfrequency values for the first mode B1x are sometimes given within intervals in the high-level case.

4.2.2. *The delicate case of high-level random tests – Nonlinearities on bending mode B1x*

FIG. 5 presents the stabilization diagrams obtained after automated modal selection when processing the data acquired during low- and high-level random tests realized after RUN16. At that stage the RC medium of the specimen has already been damaged as the drop of frequency for first bending mode B1x can testify (see TAB. 4). Inspecting the two diagrams at the top of FIG. 5 however, processing low-level random tests, one can observe the typical response of a linear structure with clear dominant low frequency content and nicely identified physical modes.

Now examining the OO stabilization diagram in the high-level case, one can clearly see a more complex modal content in the vicinity of the first eigenfrequency and more generally over the low frequency range [1 ; 10 Hz] where no real peak is to be observed on the CMIF. A large density of modes is present and the column formed by the two first eigenfrequencies are not nice nor stable, to the point that the automated selection procedure discarded the modes corresponding to T1z, classifying them as unphysical. Things are more clear regarding IO analysis where the three dominant modes are now clearly identified as physical. Examining the H-CMIF curves for both low and high-level diagrams in the IO context, one can notice that the bandwidth of the peak corresponding to B1x is wider for high-level tests. This is translated in terms of damping ratio, that is identified as 4.3 % for low-level tests, against 16.8 % in the high-level case.

Both complex modal density and really high damping level (to the limit of being considered as physical) are clear indications of the many nonlinear mechanisms that are activated by the modal movement B1x. Those non-linearities can be attributed to the swivels linking the columns to the RC specimen and table. Indeed, even though the surface of these ball joints is Teflon, solid friction forces oppose to the movement. Considering a classical Coulomb description for the moment associated to friction forces, one can distinguish two regimes:

- the swivels are locked for low level tests when the excitation is such that the torque applied on the swivels is lower than the friction threshold. Only a small relative movement is permitted (high apparent tangent stiffness is expected) and the damping ratio for mode B1x takes values ($\approx 4\%$) typical of RC constructions;
- the swivels get unlocked for high level tests when the torque applied on the swivels is greater than the friction threshold. Nonlinear Coulomb forces then participate and oppose to the movement when relative angular velocity is non-null, which leads to a dramatic increase of damping ratio for mode B1x.

Note that the same observation is made for mode T1z.

TAB. 5 collects the different results obtained for mode B1x when running OO and IO analyses for low- and high-level random tests. As was highlighted commenting FIG. 5, the complexity of interpretation of the diagrams in the OO case for the two first dominant low frequency modes has generally been observed for each high-level random test. The automated modal selection

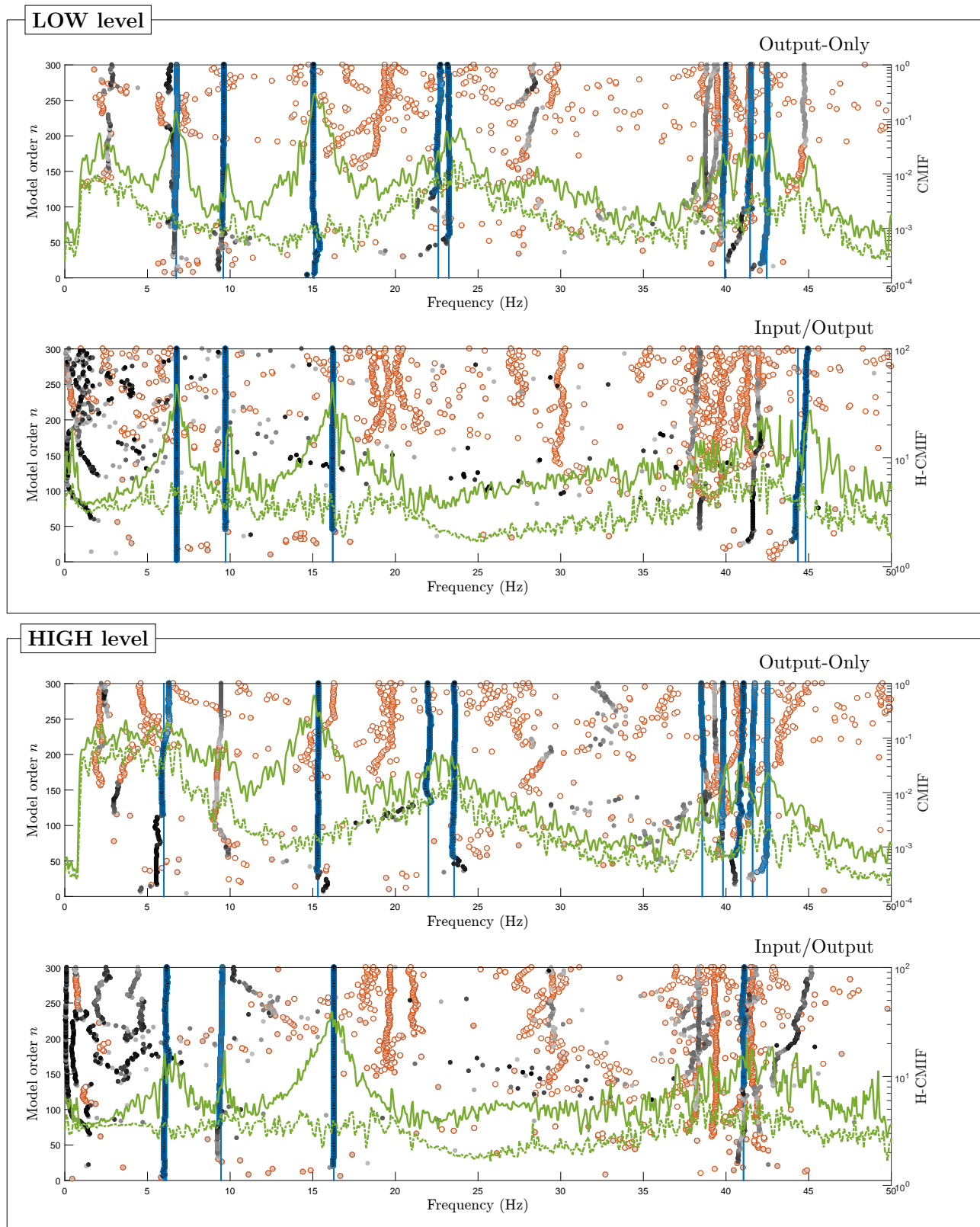


FIGURE 5: Comparison of the different analyses performed for high and low-level random tests after RUN16.

procedure derived in [13], that proved robustness with respect to non-linearity to a certain extent, sometimes failed at systematically detecting modes B1x and T1z conjointly because of generally

high damping ratio level and unstabilized modal properties. Unstabilized physical mode-columns have sometimes led to different groups after clustering for mode B1x. In TAB. 5, values are highlighted in red when manual selection replaced the automated procedure. One can notice that the automated IO analysis shows a greater degree of confidence when processing these test results.

Thus, for the first mode B1x, uncertainty on identified eigenfrequency and damping values is large in the OO case with several coexisting columns corresponding to B1x in the stabilization diagram as reported TAB. 5. In both OO and IO cases, the identified damping ratios take very high values ($\approx 20\%$ and above). Those high damping values can clearly not be related to the RC structure itself and are another clue for incriminating the swivels. This question will be addressed in details in forthcoming section 5.

Level	Analysis	Modal feat.		After RUN16	After RUN23	After RUN32	After RUN39	After RUN46	After RUN53	After RUN60				
LOW	OO	freq.	[Hz]	6.71	6.50	6.25	5.97	5.83	5.68	5.73				
		STD		0.04	0.02	0.04	0.06	0.03	0.04	0.06				
		damp.	[%]	5.7	4.4	5.5	8.3	7.0	5.6	5.1				
		STD		1.1	1.1	1.5	2.2	1.8	1.5	1.3				
	IO	freq.	[Hz]	6.76	6.46	6.30	5.95	5.76	5.61	5.57				
		STD		0.01	0.01	0.02	0.01	0.01	0.03	0.05				
		damp.	[%]	4.3	3.7	4.5	6.3	5.3	6.2	5.5				
		STD		0.1	0.1	0.2	0.2	0.3	0.7	0.2				
HIGH	OO	freq.	[Hz]	5.99	6.02	6.37	6.48	5.95	5.64	5.85	4.93	5.57	5.59	5.55
		STD		0.17	0.05	0.05	0.03	0.07	0.06	0.06	0.03	0.03	0.03	0.03
		damp.	[%]	16.6	17.8	8.7	6.0	10.9	11.3	9.2	12.8	8.0	16.5	18.4
		STD		1.3	1.3	0.7	0.5	1.6	1.4	0.7	0.8	0.7	1.5	1.1
	IO	freq.	[Hz]	6.09	5.77	5.51	5.23	5.09	4.96	4.65				
		STD		0.08	0.11	0.19	0.17	0.09	0.07	0.12				
		damp.	[%]	16.8	20.1	27.8	21.5	21.5	23.2	35.7				
		STD		1.7	1.9	3.2	1.4	1.0	1.1	6.2				

TABLE 5: Undamped frequencies and damping ratios identified for the first mode B1x after each damaging RUN. Both OO and IO analysis are realized for each low- and high-level random tests (see TAB. 1). Columns are split when several groups containing variants of the same mode B1x have been identified. Mean and standard deviation (STD) values associated to each groups are reported in the table. The mode-groups that have been missed by the automated selection procedure and manually retained are highlighted in red in the table.

4.2.3. Seismic tests – Dominant apparent frequency corresponding to mode B1x

A last attempt of using the automated 4SID methodology in an increasingly nonlinear context is now carried out. The previous subspace-based identification techniques will be applied to the seismic tests. Output-Only analysis or stochastic subspace identification relies on the strong hypotheses that the system is linear and submitted to a white noise excitation of constant covariance. For this last reason, OO analysis will not be suited for processing seismic tests. Input/Output or combined deterministic stochastic subspace identification offers more flexibility if inputs are measured, to the price of increased complexity of the identification algorithms and longer computation times (see e.g. [1]). The IO analysis is thus realized once again, specifying the three table-accelerometers recordings as inputs, but this time for the seismic tests. If the dynamic response was linear, the identified modal signature would correspond to system \mathfrak{Z}_{IO} (3). But since non-linearity is precisely expected when running seismic damaging tests (green rows of TAB. 1), the modal features extracted after analysis must be taken with care and would, in the best case, correspond to those of a linear equivalent model of system \mathfrak{Z}_{IO} . Hence, one should rather talk about dominant or apparent frequencies rather than eigenfrequencies.

FIG. 6 presents the post-processing user interface that has been developed within MATLAB[®] framework. Once again, the stabilization diagram is plotted together with the two dominant singular values of the transfer matrix $H(\omega)$ (H-CMIF green scale at the right). Compared to the IO diagrams of FIGS 4 or 5, where longer broadband random inputs of lower magnitude were applied, only a few modes with strong linear behavior are extracted by the selection procedure. Let also note that a null reference input is specified to the MTS[®] controller in the y direction, what has led to some modes having weak participation factors. One can also note that very few dispersion is observed on frequency and damping values. Displaying the modeshape contribution of mode B1x in the complex plane, one can notice a nice linear distribution of its coordinates, in accordance with the very low MPD value of 0.008 rad. This indicates that the modal response for mode B1x is organized in a rather linear manner.

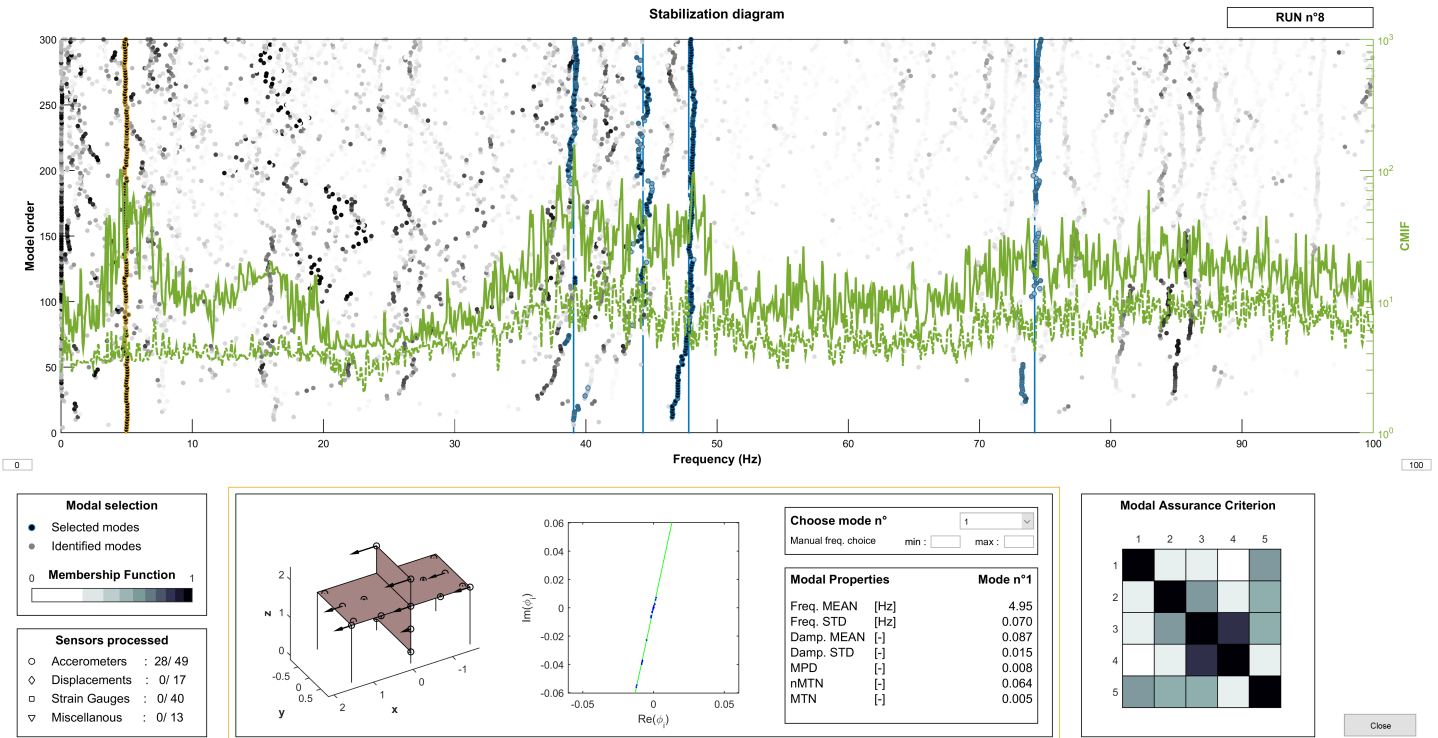


FIGURE 6: Input/Output analysis realized for seismic RUN8 – First dominant mode B1x. Post-processing user-interface window developed within MATLAB[®].

The IO analysis was repeated for each seismic run of the test campaign (green rows of TAB. 1). The dominant mode B1x has systematically been selected by the automated procedure and corresponding modeshapes have been carefully inspected. The modal features associated to B1x have been reported in TAB. 6. One shall also note that the MPD indicator keeps low values for each run (although a slight increase is observed on the two last runs), which indicates that mode B1x has been identified with a good level of confidence and seems to be a good linear approximation of the dominant behavior in the x direction.

One can appreciate the global damage of the RC specimen through the frequency drop-off. Looking at the standard deviations (STD) for both undamped frequencies and damping ratios, one can notice that the level of uncertainty is much higher for seismic tests, especially on damping. Comparing damping ratios on TABS. 5 and 6, one can also note that for the seismic tests in general, when the acceleration input is higher, the damping ratios are lower than what was identified for

Analysis	Modal feat.	RUN08	RUN12	RUN16	RUN23	RUN32	RUN39	RUN46	RUN53	RUN60
IO	freq.	4.95	4.29	3.17	2.65	2.47	2.28	1.98	1.79	1.76
	STD [Hz]	0.07	0.25	0.06	0.05	0.10	0.03	0.06	0.09	0.10
	damp.	8.7	13.2	10.9	11.2	8.9	9.8	8.2	15.5	31.7
	STD [%]	1.5	4.7	1.9	1.3	2.6	1.7	2.8	4.5	5.4
	MPD [rad]	0.008	0.018	0.006	0.006	0.010	0.011	0.010	0.030	0.031

TABLE 6: Undamped frequencies and damping ratios identified for the first mode B1x for each damaging RUN.

high level random tests. This will be discussed in details in the following section 5. The damping ratio keeps relatively constant values around $\approx 8\%$ and reaches values up to more than 30% at the end of the test campaign for RUN60. The same kind of observation can be done on TAB. 5 when looking at IO-processed high level random tests results. This is an indication that new dissipative phenomena are involved due to apparition of cracks in the RC medium: friction between crack-lips or at steel rebars/concrete matrix interface might be the cause for this important damping increase.

Anyhow, even if damaging nonlinear mechanisms activate during the seismic test, a certain robustness of the IO-4SID procedure is experienced for seismic tests. Let one note that the damage increase from a seismic test to the next one is moderate; besides frequency drop-off, the nonlinear mechanisms are mostly translated into a damping ratio increase, two phenomena that subspace-based identification is able to capture.

5. Analytical modelling and discussion – Nonlinear behavior of the swivels

For high-level random tests, the identified damping ratios are very high for mode B1x (above 20% for some tests) and could, in other context, have been interpreted as unphysical. The damping ratios given in TAB. 5 and 6 must then be taken with care and one shall be aware that given ratios are related to equivalent apparent damping. One could also wonder why the apparent damping ratios are generally higher for random tests than for higher PGA seismic runs. In fact, comparatively to the ground motion intensity (see TAB. 1 for PGA levels comparison), the friction forces in the swivels play a more important role for (high-level) random tests than for seismic runs, which leads to higher damping ratios. In order to back up this interpretation, a simple model containing one DOF is studied in this section.

Let one consider the simple uniaxial model of FIG. 7. The dynamical response of the poly-articulated RC structure is described using a nonlinear oscillator containing a single observable DOF x , with corresponding mass m , that represents the modal contribution of the dominant first mode B1x. The couple (k, ξ) stands for the (modal) stiffness and viscous damping term of the RC structure (in blue). A second non-dissipative element, of stiffness k_R , is added in parallel to account for both initial tangent stiffness of the swivels around y -axis and the rods stiffnesses themselves (in green). The non-linearity is handled by introducing a second internal degree of freedom θ standing for the relative angular displacement in the swivels and a Coulomb-type friction law is used for modeling the locked/unlocked behavior of the swivels.

The constitutive relations for this nonlinear oscillator are given by:

$$\left. \begin{aligned} \ddot{x} + 2\xi_1\omega_1\dot{x} + \omega_1^2x + \omega_R^2(x - \theta) &= -\Gamma \\ \omega_R^2(x - \theta) + g_{NL} &= 0 \end{aligned} \right\} \quad \text{with} \quad \begin{cases} \text{Static friction :} & \dot{\theta} = 0 \quad \text{if } |g_{NL}| < g_0 \\ \text{Sliding :} & g_{NL} = -g_0 \operatorname{sgn}(\dot{\theta}) \quad \text{if } |\dot{\theta}| > 0 \end{cases} \quad (6)$$

where g_{NL} stands for the nonlinear restoring force, applied in point O , and follows the classical Coulomb-friction description with *sliding* and *static friction* conditions.

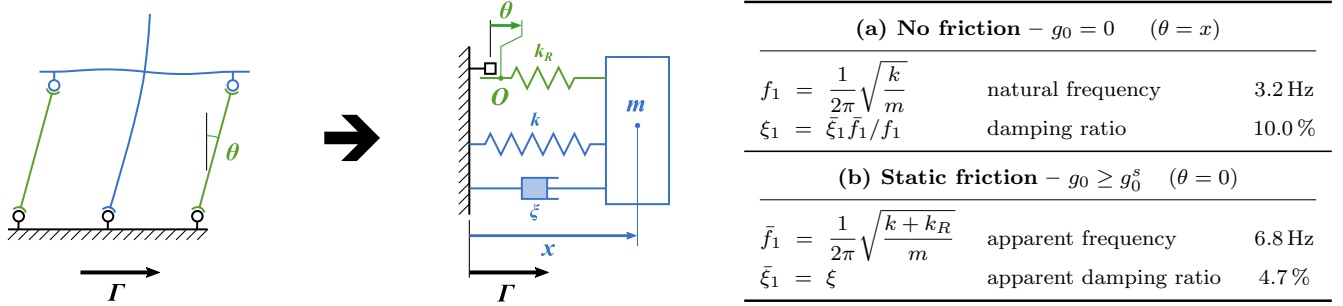


FIGURE 7: Simple nonlinear model with friction used for describing the dominant mono-modal response (first mode).

The structural parameters of the nonlinear oscillator (see FIG. 7) are chosen such as resembling the characteristics experimentally identified for RUN16. Let one note that the dynamical equilibrium in eq. (6) is written under canonical form; this implies that the Coulomb force g_{NL} and its corresponding threshold g_0 are not homogenous to forces, but to accelerations.

The acceleration of the support is defined as a white noise sequence and normalized such that $\max_{t \in [0; T]} |\Gamma(t)| = 1$. Using this last normalization, the friction threshold g_0 is the only parameter that rules the ‘degree of non-linearity’ of the oscillator. Depending on the value of g_0 , two asymptotic linear behaviors can be distinguished:

- (a) No friction – $g_0 \approx 0$: the swivels are unlocked ($\theta = x$) with negligible ratio of friction forces opposing to the sliding movement. The observed dynamics corresponds to this of a simple oscillator of characteristics ($f_1 = \sqrt{k/m}$, ξ_1);
- (b) Static friction – $g_0 \geq g_0^s$: when the friction threshold exceeds a certain value g_0^s (w.r.t. input Γ), the swivels are locked ($\theta = 0$) on the entire interval $[0; T]$. The behavior of the oscillator is linear but the apparent frequency and damping are changed because of the stiffness k_R operating in parallel to yield:

$$\bar{f}_1 = \frac{1}{2\pi} \sqrt{\frac{k + k_R}{m}} \quad \text{and} \quad \bar{\xi}_1 = \xi_1 \frac{f_1}{\bar{f}_1} \quad (7)$$

The damping value identified from low-level random tests after RUN16 (see TAB. 5) with locked swivels is taken as reference $\bar{\xi}_1 = 4.7\%$. Also note that the oscillator of FIG. 7 corresponds to a uniaxial elasto-plastic model with linear kinematic hardening, with θ playing the role of a plastic strain and g_0 of a plasticity threshold.

The acceleration sequence is sampled at frequency $f_s = 1000$ Hz, with null initial and final values and the system (6) is simulated using a Newmark scheme, with classical ($\beta = 1/4$, $\gamma = 1/2$) parameters. A quasi-Newton algorithm is used for handling the constitutive relation non-linearity (minimization of the equilibrium residual, see classical reference [48] for details). Absolute accelerations are processed writing $y = \ddot{x} + \Gamma$ and a white noise w is added to simulated accelerations to account for measurement noise such that $w = 0.05n$ and $n \sim \mathcal{N}(0, 1)$.

FIG. 8 shows the PSD and Transfer Function (TF) of the absolute acceleration response of mass m w.r.t. ground motion input Γ for varying values of g_0 . A classical Welch’s windowing

with 2000 non-overlapping 5 s-long rectangular segments is used for computing the PSDs and TFs. One can notice on FIG. 8, in bold grey, the linear responses corresponding to asymptotic values (a) $g_0 = 0$ and (b) $g_0 = g_0^s$ and, in colors, a clear increase of the apparent damping (peaks flattening) for values $g_0 \in]0; 0.3[$ due to the larger proportion of friction forces involved. Regarding the frequency content, it seems to be clearly dominated by a single frequency for values of g_0 close to the asymptotic values 0 and 0.3. The same observation is made for intermediate values of g_0 where a clear mono-modal behavior is observed together with a large increase of the apparent damping ratio. Note that classical plasticity (with usual ductility demand parameter, see [35]) would correspond to values of g_0 within $[0.1; 0.3]$.

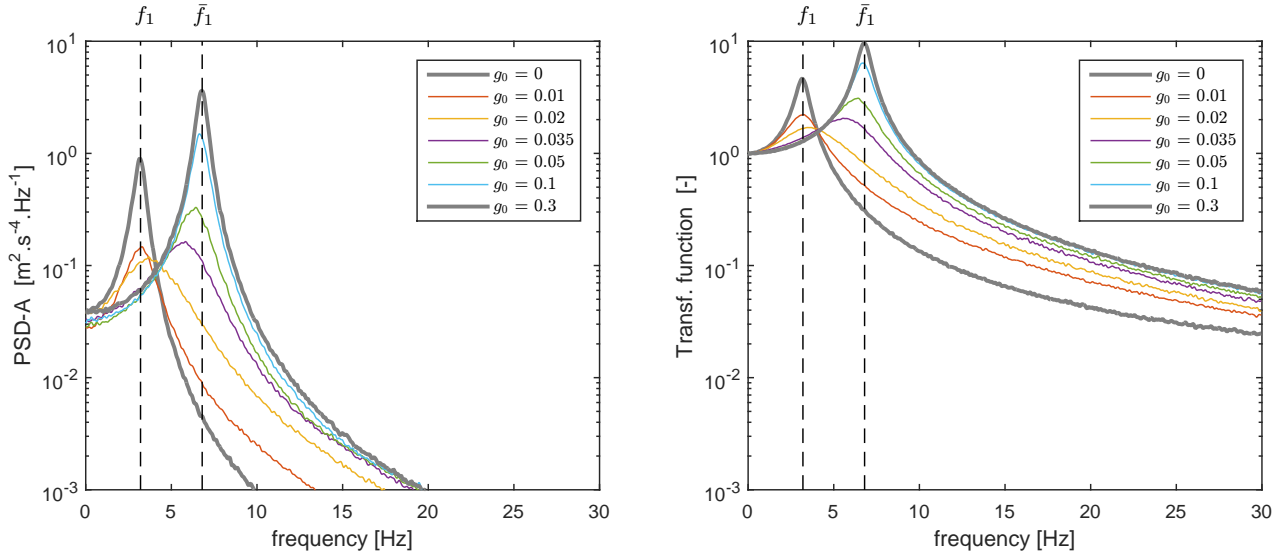


FIGURE 8: Acceleration response of the simple model to an adimensional white noise Γ in terms of Power Spectral Density (left) and Transfer Function (right) for varying friction threshold g_0 .

In order to take a critical look at the studies carried out so far on the JVP database, it is necessary to assess how the OO and IO subspace algorithms behave when facing known and increasing Coulomb-friction non-linearity. The CVA-algorithm in the OO case and combined deterministic-stochastic algorithm in the IO case have been carried out on the simulated measurements of length $T = 120$ s for varying values of g_0 . TAB. 7 presents the stabilization diagrams and dominant mode selected for different values of g_0 . When processing data for which the proportion of friction forces is high with respect to input level (see TAB. 7, $g_0 = 0.035$), the complex modal density around the dominant frequency, observed when processing low-level random tests after RUN16 (see FIG. 5), is well reproduced, especially in the OO case. In order to quantify the performance of each procedure on this simulated example, a ratio r of identification is computed for the dominant mode. The ratio $r \triangleq \text{card} \Omega_1^{ph} / J_{max}$ is defined as the number of actually identified modes (cardinal of the group Ω_1^{ph} built after automated procedure described in [13]) divided by the maximum expected number of modes in Ω_1^{ph} (specifying $n \in \{2, 4, \dots, n_{max}\}$, we have $J_{max} = n_{max}/2$). A ratio of $r = 100\%$, as can be observed in the linear case, means that the mode is clearly identified for each model order n . Lower values of r indicate the difficulty of the subspace algorithm to identify the dominant mode. As can be observed in TAB. 7, focusing on ratio r , OO and IO algorithms behave similarly in the linear case, whereas IO algorithm provides more populated physical groups Ω_1^{ph} with ratios r closer to 100%.

TAB. 8 in turn presents the values identified for dominant frequency \bar{f} and damping ratio $\bar{\xi}$

for varying values of threshold g_0 . Dispersion obtained on apparent frequency and damping ratio is generally higher when OO identification is used and seems to involve more outliers.

FIG. 9 shows the evolution of the apparent damping $\bar{\xi}$ w.r.t. the rate of nonlinear forces g_0 predicted by the sDOF nonlinear oscillator and analyzed in the IO framework (see TAB. 8); experimental values associated to mode B1x and identified for different RUNs are added for comparison². The damping values identified for RUN16 and following random tests are coherent with the ratios predicted by the simple nonlinear oscillator.

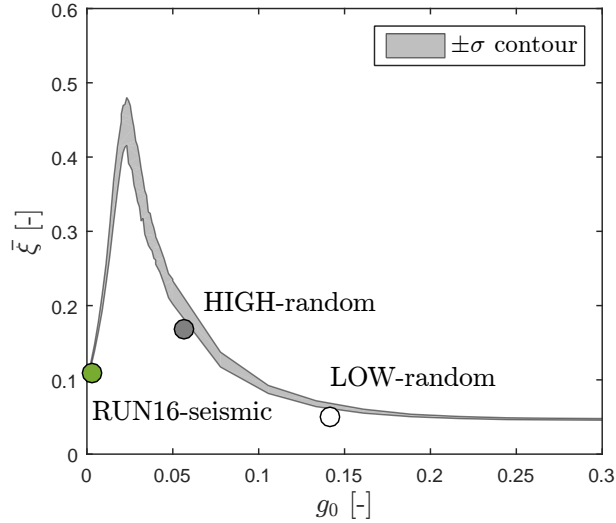


FIGURE 9: Apparent damping predicted by sDOF nonlinear oscillator (gray fill) vs. experimental values identified for RUN16 and consecutive low- and high-level random tests.

When dealing with multi-DOFs systems with nonlinear mechanisms, stationary periodic content can appear in the output spectra as a result of the interaction between modes (see e.g. [30] for details on NNMs and pole combination for dynamic systems with quadratic or cubic stiffness). A numerical study involving a 2-DOFs nonlinear system has also been conducted for questioning the presence of nonlinear modes when facing such kind of Coulomb-friction non-linearity. The constitutive relations of the 2-DOFs oscillator were calibrated such as representing the modal behavior associated to the two first dominant modes B1x and T1z. No pole combination phenomena were to be observed for this second case and the conclusions on the relative performance of the OO and IO approaches are similar to those of the sDOF case. This study is available in appendix D for the interested reader.

6. Conclusions

In this paper, feedback is provided on the possibility of using subspace-based modal identification techniques in the presence of both structural damage and Coulomb-friction (or elasto-

²According to the definition of g_0 in eq. (6), neglecting the viscoelastic restoring force from k_R , k and ξ when sliding occurs, one can roughly consider that the moment of inertia forces is balanced by the torque C_0 associated to solid friction forces at swivels. A coarse estimation of the experimental threshold can then be given writing $g_0 \propto \frac{C_0}{mgH \max_t \Gamma(t)}$, from the knowledge of experimentally measured C_0 , total mass m of the specimen (including rods, swivels and additional masses) and gravitational constant g .

plasticity). More precisely, a three-stage automated selection procedure was carried out on both experimental and simulated measurements in the OO and IO context such that the subspace-based algorithm are confronted with increasing non-linearity. Experimental results from shaking table tests on embedded RC structure anchored using nonlinear swivels with solid friction have been processed. Both numerical and experimental studies highlighted the robustness of the modal selection process and subspace-based identification algorithm in general when facing Coulomb-friction non-linearity. The dynamic response of the studied specimen could have been qualified as ‘modal’ (at least in the low frequency range) with clear dominant frequency behavior and increased apparent modal damping ratio when non-linearity was involved. Note however that certain lack of precision have been experienced when processing the experimental database because of too short duration of measurements (30 s-long recordings sampled at 512 Hz). For both experimental and numerical datasets, slightly clearer results have been obtained with IO algorithms. Robustness has also been experienced with respect to the damage process when performing IO analysis for seismic tests of increasing level, provided that damage increment between two tests is moderate.

Regarding friction independently, depending on the ratio between input ground-motion magnitude and expected nonlinear forces, high damping ratios have been identified, possibly higher than 20 %, both in the numerical and experimental case. Current practice when resorting to automated procedure for clarifying stabilization diagrams consists in discarding the modes with more than 20 % damping that are interpreted as unphysical (hard-validation criteria). In the application considered in this paper, dominant modal content would have been missed, what stresses the importance of having a modal selection procedure that can adapt to the data content, with ideally no thresholding, for offering more flexibility.

Anyhow, the present work illustrates that studying the modal response of systems containing elastoplastic components (with hardening) or equivalently nonlinear dissipative subsystems of Coulomb-friction type operating in parallel of structural stiffness is possible and meaningful using linear identification techniques, like subspace-based algorithms. Yielding results can provide relevant linear equivalent approximations for such kind of non-linearity.

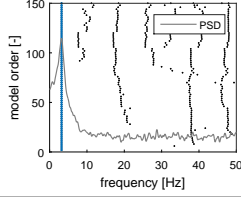
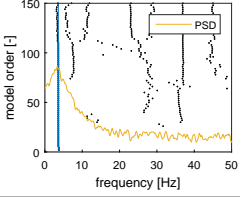
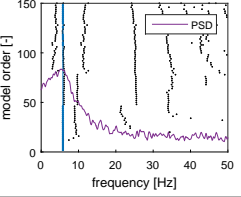
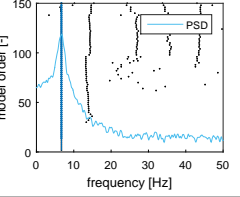
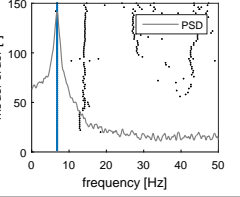
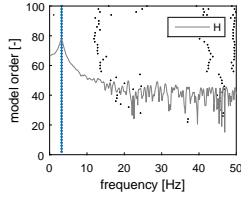
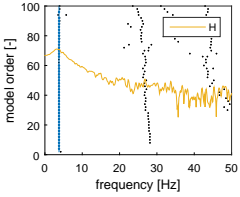
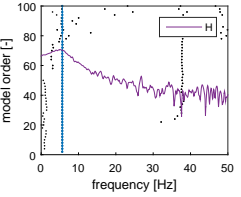
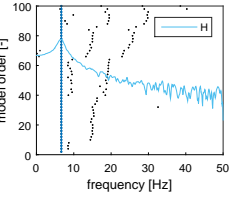
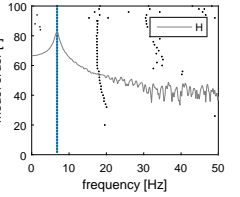
Analysis	(a) No friction	Kinematic friction – Increased apparent damping			(b) Static friction	
	$g_0 = 0$	$g_0 = 0.02$	$g_0 = 0.035$	$g_0 = 0.1$	$g_0 \geq g_0^s = 0.3$	
OO						
	\bar{f} [Hz]	3.19	3.59	5.82	6.70	6.82
	$\bar{\xi}$ [%]	10.25	42.31	34.04	8.65	4.21
	r [%]	100.0	70.7	52.0	92.0	100.0
IO						
	\bar{f} [Hz]	3.20	3.78	5.66	6.67	6.80
	$\bar{\xi}$ [%]	10.13	44.13	33.52	9.87	4.76
	r [%]	100.0	88.0	94.0	100.0	100.0
Linearity	✓	✗	✗	✗	✓	
Targeted	\bar{f} [Hz]	3.20	–	–	–	6.80
	$\bar{\xi}$ [%]	10.00	–	–	–	4.71

TABLE 7: Single DOF nonlinear oscillator – IO vs. OO results in terms of apparent frequency and damping ratio for different friction load ratios g_0 . The rate r (see text for definition) quantifies the ability of the procedures to retain the dominant mode as physical. (a) No friction, linear asymptotic case with $\theta = x$. (b) Static friction, linear asymptotic case with no relative movement $\theta = 0$.

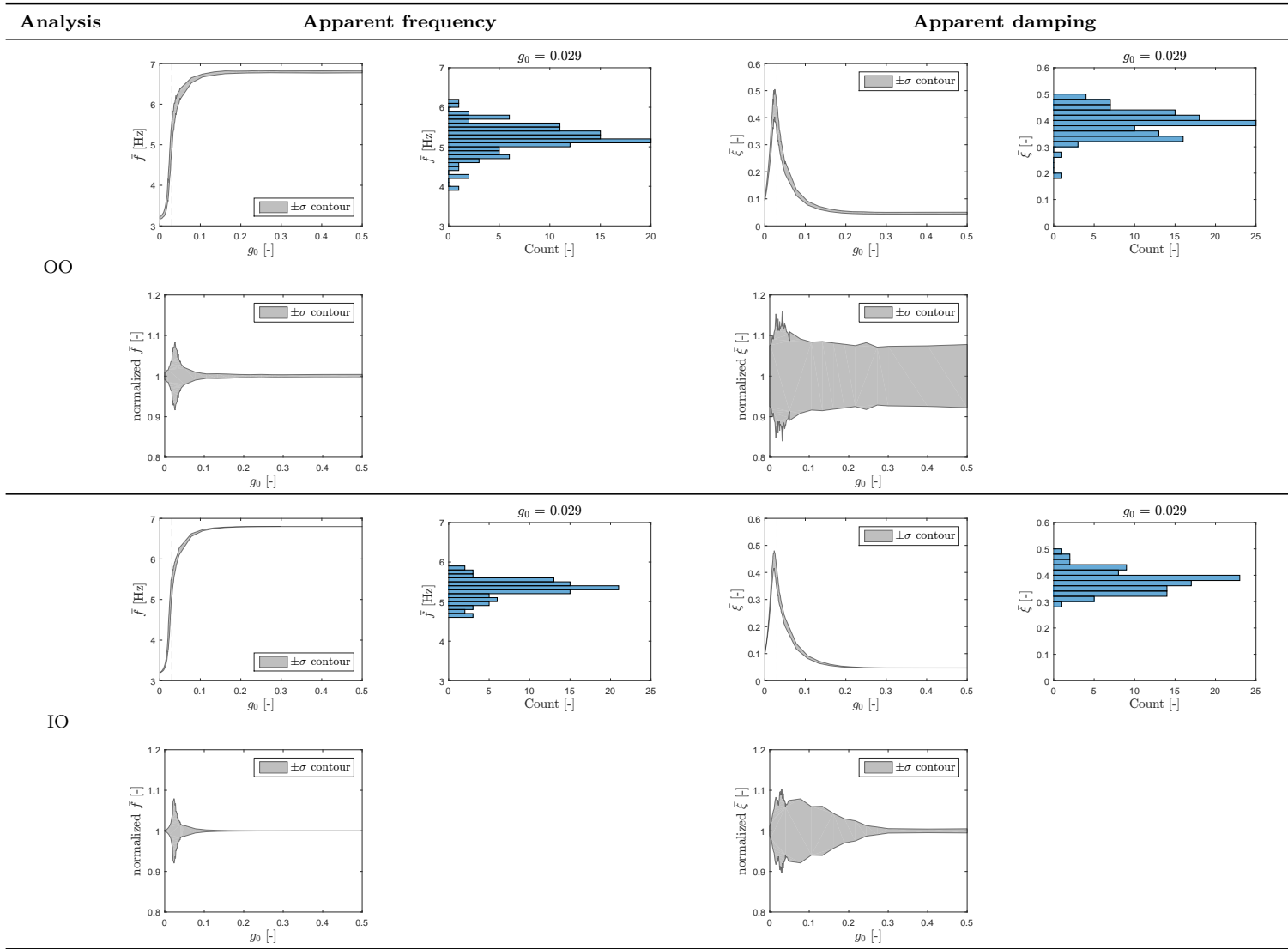


TABLE 8: Single DOF oscillator – Dispersion on the identified modal features for OO and IO procedures.

In each case, for each value of $g_0 \in [0; 0.5]$, 120 dynamic responses of the same oscillator to different realizations of the white-noise input are processed using OO and IO subspace-based identification algorithms. Gray fills represent the $\pm\sigma$ covariance envelope for different identified features for varying threshold g_0 . The histograms are related to the dispersion obtained for $g_0 = 0.029$, value marked with dotted line on subsequent plots. The normalized plots are adimensionalized w.r.t. mean value of corresponding feature.

Acknowledgments

The tandem EDF-CEA is deeply acknowledged for funding this research activity and giving access to the JVP database. The work reported in this paper has been also supported by the SEISM Institute. F. Wang (CEA), H. Oliveira, E. Hervé-Secourgeon (EDF) and F. Voldoire (EDF) are more personally thanked for the fruitful discussions. Th. Chaudat (CEA) is also thanked for transmitting the mandatory details about the test campaign.

References

- [1] P. Van Overschee and B. De Moor. *Subspace Identification for Linear Systems : Theory, Implementation, Applications*. Kluwer Academic Publishers, 1996.
- [2] Michèle Basseville, Albert Benveniste, Maurice Goursat, Luc Hermans, Laurent Mevel, and Herman Van der Auweraer. Output-only subspace-based structural identification: From theory to industrial testing practice. *Journal of Dynamic Systems, Measurement, and Control*, 123(4):668–676, feb 2001.
- [3] Arnaud Deraemaeker and Keith Worden, editors. *New Trends in Vibration Based Structural Health Monitoring*. Springer, 2010.
- [4] Filipe Magalhães and Álvaro Cunha. Explaining operational modal analysis with data from an arch bridge. *Mechanical Systems and Signal Processing*, 25(5):1431–1450, jul 2011.
- [5] K. Worden, C. R. Farrar, G. Manson, and G. Park. The fundamental axioms of structural health monitoring. *Proceed. R. Soc. A, Math. Phys. Eng. Sci.*, 2007.
- [6] J. M. W. Brownjohn. Structural health monitoring of civil infrastructure. *Proceed. R. Soc. A, Math. Phys. Eng. Sci.*, 2007.
- [7] Johan Maeck, Bart Peeters, and Guido De Roeck. Damage identification on the Z24 bridge using vibration monitoring. *Smart Materials and Structures*, 10(3):512–517, jun 2001.
- [8] Edwin Reynders and Guido De Roeck. Continuous vibration monitoring and progressive damage testing on the Z24 bridge. In *Encyclopedia of Structural Health Monitoring*. Wiley, jan 2008.
- [9] Edwin Reynders, Gersom Wursten, and Guido De Roeck. Output-only structural health monitoring in changing environmental conditions by means of nonlinear system identification. *Structural Health Monitoring*, 13(1):82–93, oct 2013.
- [10] Edwin Reynders and Guido De Roeck. Vibration-based damage identification: The Z24 bridge benchmark. In *Encyclopedia of Earthquake Engineering*, pages 1–8. Springer Berlin Heidelberg, 2014.
- [11] F. Ubertini, N. Cavalagli, A. Kita, and G. Comanducci. Assessment of a monumental masonry bell-tower after 2016 central italy seismic sequence by long-term shm. *Bulletin of Earthquake Engineering*, 16:775–801, 2018.

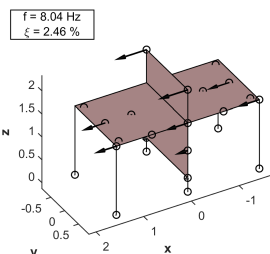
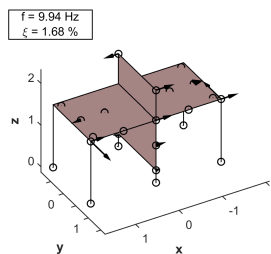
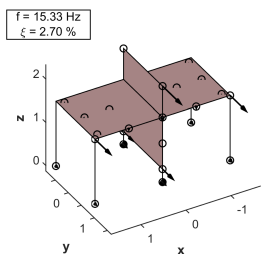
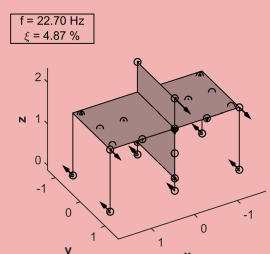
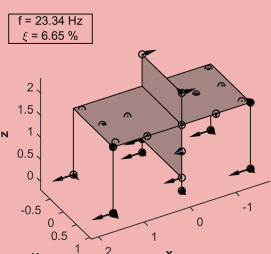
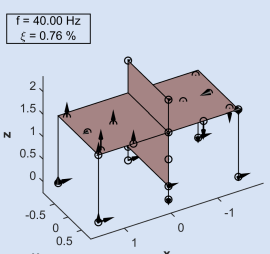
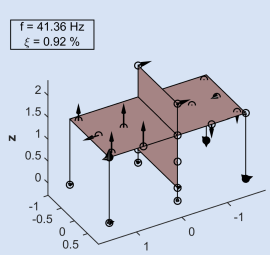
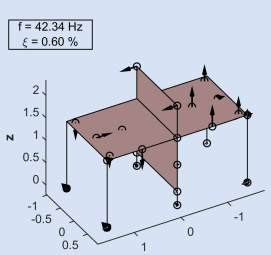
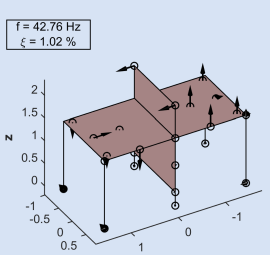
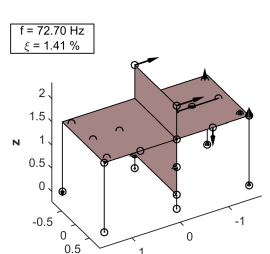
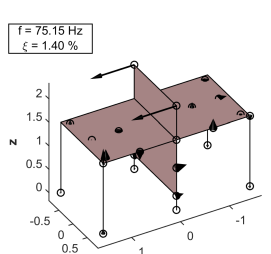
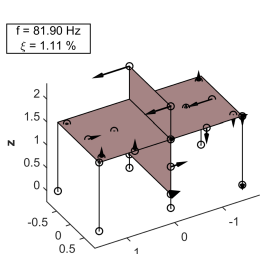
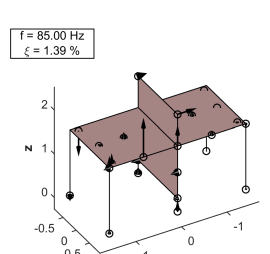
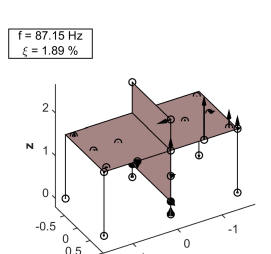
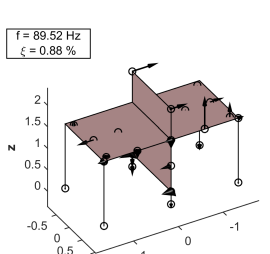
- [12] Giuseppe Lacidogna, Gianfranco Piana, Federico Accornero, and Alberto Carpinteri. Multi-technique damage monitoring of concrete beams: Acoustic emission, digital image correlation, dynamic identification. *Construction and Building Materials*, 242:118114, may 2020.
- [13] P.-É. Charbonnel. Fuzzy-driven strategy for fully automated modal analysis: Application to the SMART2013 shaking-table test campaign. *Mechanical Systems and Signal Processing*, 152:107388, may 2021.
- [14] Bart Peeters and Guido De Roeck. One-year monitoring of the Z24-bridge: environmental effects versus damage events. *Earthquake Engineering and Structural Dynamics*, 30(2):149–171, 2001.
- [15] E.J. Cross, K.Y. Koo, J.M.W. Brownjohn, and K. Worden. Long-term monitoring and data analysis of the tamar bridge. *Mechanical Systems and Signal Processing*, 35(1-2):16–34, feb 2013.
- [16] C. Rainieri and G. Fabbrocino. Development and validation of an automated operational modal analysis algorithm for vibration-based monitoring and tensile load estimation. *Mechanical Systems and Signal Processing*, 60-61:512–534, 2015.
- [17] C. Gentile, A. Ruccolo, and F. Canali. Long-term monitoring for the condition-based structural maintenance of the milan cathedral. *Construction and Building Materials*, 228:117101, 2019.
- [18] Michèle Basseville, Maher Abdelghani, and Albert Benveniste. Subspace-based fault detection algorithms for vibration monitoring. *Automatica*, 36(1):101–109, jan 2000.
- [19] L. Mevel, M. Basseville, and A. Benveniste. Fast in-flight detection of flutter onset: A statistical approach. *Journal of Guidance, Control, and Dynamics*, 28(3):431–438, 2005.
- [20] Mingyi Huo, Hao Luo, Shen Yin, Yuchen Jiang, and Okyay Kaynak. A novel subspace-aided fault detection approach for the drive systems of rolling mills. *IEEE Transactions on Control Systems Technology*, 30(4):1742–1749, jul 2022.
- [21] M. Basseville, L. Mevel, and M. Goursat. Statistical model-based damage detection and localization: subspace-based residuals and damage-to-noise sensitivity ratios. *Journal of Sound and Vibration*, 275(3-5):769–794, aug 2004.
- [22] E. Balmès, M. Basseville, L. Mevel, H. Nasser, and W. Zhou. Statistical model-based damage localization: A combined subspace-based and substructuring approach. *Structural Control and Health Monitoring*, 15(6):857–875, oct 2008.
- [23] Dionisio Bernal. Load vectors for damage location in systems identified from operational loads. *Journal of Engineering Mechanics*, 136(1):31–39, jan 2010.
- [24] Luciano Marin, Michael Döhler, Dionisio Bernal, and Laurent Mevel. Robust statistical damage localization with stochastic load vectors. *Structural Control and Health Monitoring*, 22(3):557–573, sep 2014.
- [25] Michael Döhler, Laurent Mevel, and Qinghua Zhang. Fault detection, isolation and quantification from gaussian residuals with application to structural damage diagnosis. *Annual Reviews in Control*, 42:244–256, 2016.

- [26] E. Zhang, R. Pintelon, and P. Guillaume. Modal identification using OMA techniques: Non-linearity effect. *Shock and Vibration*, 2015:1–12, 2015.
- [27] E. Neu, F. Janser, A. A. Khatibi, and A. C. Orifici. Fully automated operational modal analysis using multi-stage clustering. *Mechanical Systems and Signal Processing*, 84:308–323, 2017.
- [28] S.W. Shaw and C. Pierre. Normal modes for non-linear vibratory systems. *Journal of Sound and Vibration*, 164(1):85–124, jun 1993.
- [29] Alexander F. Vakakis. *Normal modes and localization in nonlinear systems*. Wiley series in nonlinear science. Wiley, New York, 1996.
- [30] K. Worden and G. R. Tomlinson. Nonlinearity in experimental modal analysis. *Philosophical Transactions of the Royal Society of London. Series A: Mathematical, Physical and Engineering Sciences*, 359(1778):113–130, jan 2001.
- [31] Gaëtan Kerschen, Keith Worden, Alexander F. Vakakis, and Jean-Claude Golinval. Past, present and future of nonlinear system identification in structural dynamics. *Mechanical Systems and Signal Processing*, 20(3):505–592, apr 2006.
- [32] Walter Lacarbonara, Biagio Carboni, and Giuseppe Quaranta. Nonlinear normal modes for damage detection. *Meccanica*, 51(11):2629–2645, jun 2016.
- [33] Th. Chaudat, E. Hervé-Secourgeon, F. Voldoire, F. Wang, S. Magne, S. Rougeault, R. Desmarchelier, A. Guilloux, F. Gatuingt, and C. Oliver-Leblond. Bending behaviour and robustness under seismic loading conditions of reinforced concrete wall-slab connections. test description and experimental observations. (*submitted to Nuclear Engineering and Design*), 2022.
- [34] T. K. Caughey. Random excitation of a system with bilinear hysteresis. *Journal of Applied Mechanics*, 27(4):649–652, dec 1960.
- [35] Ioannis Politopoulos and Cyril Feau. Some aspects of floor spectra of 1dof nonlinear primary structures. *Earthquake Engineering & Structural Dynamics*, 36(8):975–993, 2007.
- [36] Hugo Oliveira, François Louf, Estelle Hervé-Secourgeon, and Fabrice Gatuingt. Wall-slab joint parameter identification of a reinforced concrete structure using possibly corrupted modal data. *International Journal for Numerical and Analytical Methods in Geomechanics*, 44(1):19–39, nov 2019.
- [37] Thierry Chaudat. Comportement sismique des jonctions voile/plancher – rapport des essais flexion dynamique. Technical report, 2020.
- [38] H. G. Harris and G. Sabnis. *Structural Modeling and Experimental Techniques*. CRC Press, 2nd edition edition, mar 1999.
- [39] P. Stoica and R. Moses. *Spectral analysis of signals*. Prentice Hall, 2004.

- [40] Estelle Secourgeon. *Caractérisation et modélisation du comportement des jonctions voile-plancher en béton armé pour l'analyse sismique des ouvrages de Génie Civil et des équipements*. PhD thesis, 2020. Thèse de doctorat dirigée par Gatuingt, Fabrice Génie civil université Paris-Saclay 2020.
- [41] Bart Peeters and Guido De Roeck. Reference-based stochastic subspace identification for output-only modal analysis. *Mechanical Systems and Signal Processing*, 13(6):855 – 878, 1999.
- [42] E. Reynders, J. Houbrechts, and G. De Roeck. Fully automated (operational) modal analysis. *Mechanical Systems and Signal Processing*, 29:228–250, 2012.
- [43] A. Benveniste and L. Mevel. Nonstationary consistency of subspace methods. *IEEE Transactions on Automatic Control*, 52(6):974–984, June 2007.
- [44] E. Reynders and G. De Roeck. Reference-based combined deterministic-stochastic subspace identification for experimental and operational modal analysis. *Mechanical Systems and Signal Processing*, 22:617–637, 2008.
- [45] C. Y. Shih, Y. G. Tsuei, R. J. Allemang, and D. L. Brown. Complex mode indication function and its applications to spatial domain parameter estimation. *Mechanical Systems and Signal Processing*, 2(4):367–377, October 1988.
- [46] T. K. Hasselman. Modal coupling in lightly damped structures. *AIAA Journal*, 14:1627–1628, 1976.
- [47] D. J. Ewins. *Modal Testing : Theory, Practice and Application*. Research Studies Press, Baldock, Hertfordshire, UK, 2000.
- [48] M. Géradin and D. Rixen. *Mechanical Vibrations*. Wiley, 2nd edition, 1997.

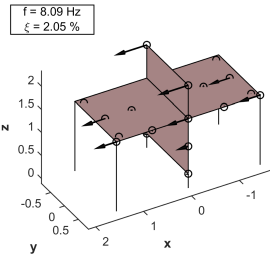
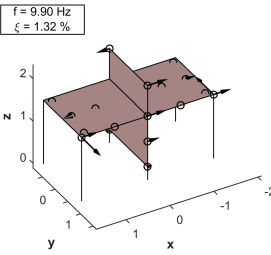
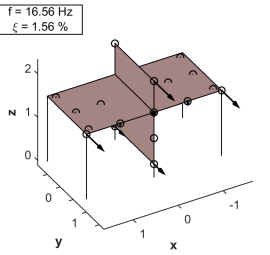
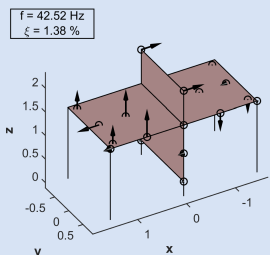
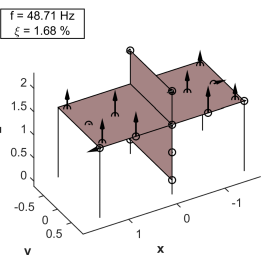
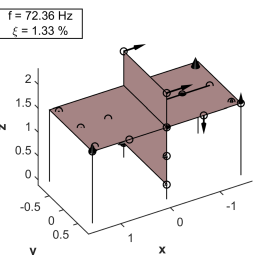
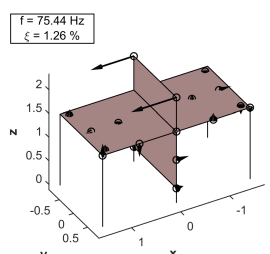
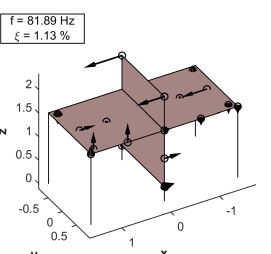
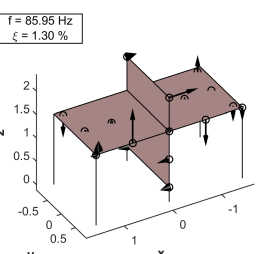
Appendix A Modeshapes identified in the OO context for eigenfrequencies on the range [0; 100 Hz] after RUN08

TABLE 9: Experimental modeshapes – OO analysis after RUN08 – Stab. diagram FIG. 4 (Top).

Mode	Modeshape	Mode #	Modeshape	Mode #	Modeshape
B1x		T1z		R1y	
Hy		Hx		B2x+E*	
B2x+E*		B2x+E*		B2x+E*	
B3x+E*		B3x		F1z	
F2z		F2z+E5x		B4x	

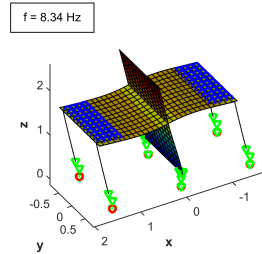
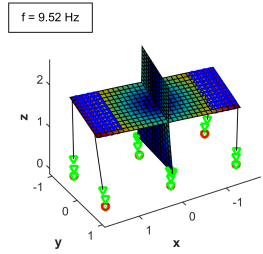
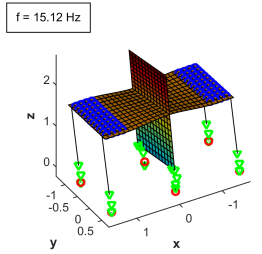
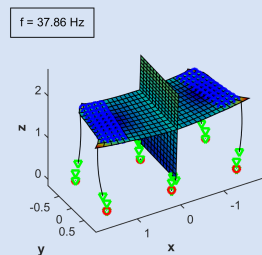
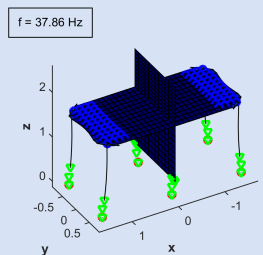
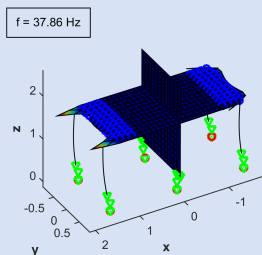
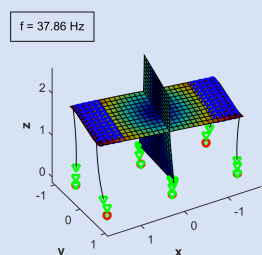
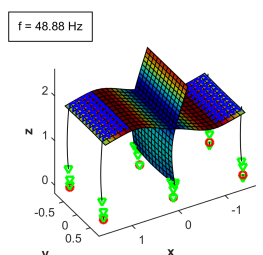
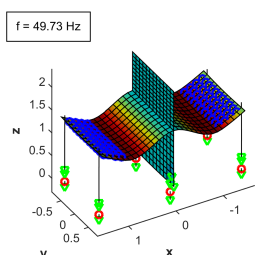
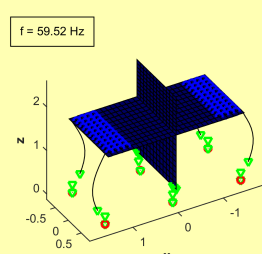
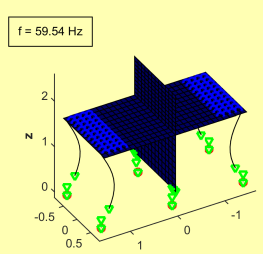
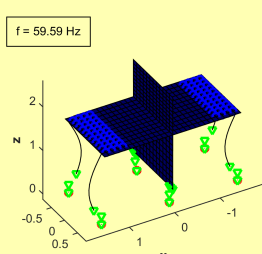
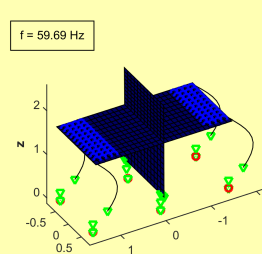
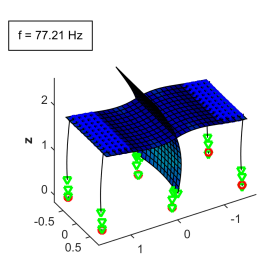
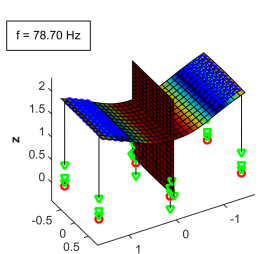
Appendix B Modeshapes identified in the IO context for eigenfrequencies on the range [0 ; 100 Hz] after RUN08

TABLE 10: Experimental modeshapes – IO analysis after RUN08 – Stab. diagram FIG. 4 (Bottom).

Mode	Modeshape	Mode #	Modeshape	Mode #	Modeshape
B1x		T1z		R1y	
B2x+E*		S1z		B3x+E*	
B3x		F1z		F2z	

Appendix C Numerical modeshapes of the linear FE model derived in [36]

TABLE 11: Numerical modeshapes of the linear FE model derived in [36] on the range [0; 150 Hz].

Mode #	Modeshape	Mode #	Modeshape	Mode #	Modeshape
B1x		T1z		R1y	
E1x		E2x		E3x	
E4x		B2x		S1z	
R1x		R2x		R3x	
R4x		B3x		S2z	

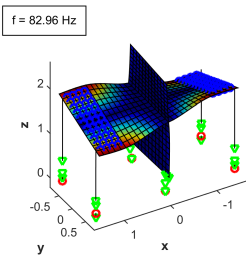
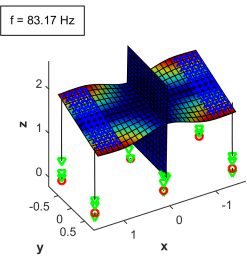
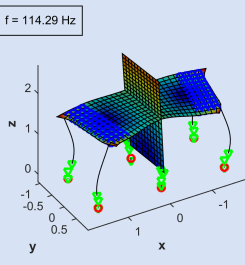
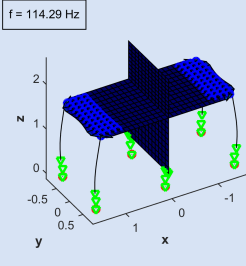
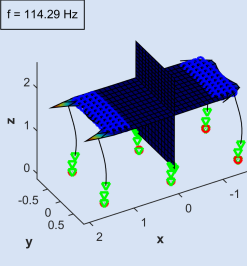
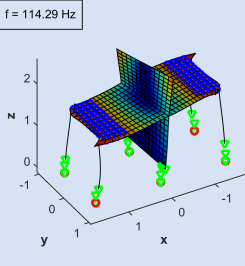
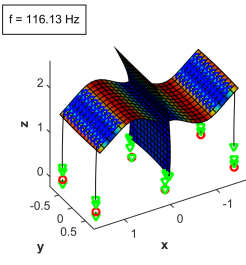
Mode	Modeshape	Mode #	Modeshape	Mode #	Modeshape
F1z		F2z		E5x	
E6x		E7x		E8x	
B4x					

TABLE 11: Numerical modeshapes of the linear FE model derived in [36] on the range $[0; 150 \text{ Hz}]$.

Appendix D Two DOFs model with Coulomb-friction

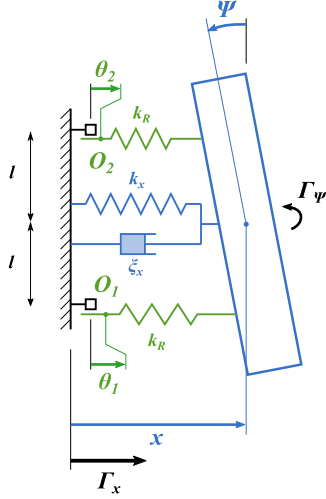
When dealing with dynamic response of multi-DOFs nonlinear systems with high expected damping values, questioning the presence of nonlinear modes or coupling between modes as well as the ability of subspace-based algorithms to distinguish them is legitimate. In order to provide substantial elements of response, the two DOFs model of FIG. 11 is considered. This time two internal variables θ_1 and θ_2 are introduced. The dynamic equilibrium (with unitary mass and inertia term) of the system reads:

$$\ddot{x} + 2\xi_1\omega_1\dot{x} + \omega_1^2x - \underbrace{\omega_R^2(\theta_1 - x - \psi l)}_{g_1} - \underbrace{\omega_R^2(\theta_2 - x + \psi l)}_{g_2} = -\Gamma_x \quad (8)$$

$$\ddot{\psi} + 2\xi_2\omega_2\dot{\psi} + \omega_2^2\psi - \underbrace{\omega_R^2(\theta_2 - x - \psi l)}_{g_1}l + \underbrace{\omega_R^2(\theta_1 - x + \psi l)}_{g_2}l = -\Gamma_\psi \quad (9)$$

where g_1 and g_2 are the nonlinear restoring forces, operating in O_1 and O_2 (see FIG. 10), and obeying to the following friction conditions:

$$\forall i = 1, 2 \quad \begin{cases} \text{Static friction :} & \dot{\theta}_i = 0 \quad \text{if } |g_i| < g_0 \\ \text{Sliding :} & g_i = -g_0 \operatorname{sgn}(\dot{\theta}_i) \quad \text{if } |g_i| > g_0 \end{cases} \quad (10)$$



No friction - $g_0 = 0$		
$f_1 = \frac{1}{2\pi} \sqrt{\frac{k_x}{m}}$	natural frequency	3.2 Hz
$\xi_1 = \bar{\xi}_1 \bar{f}_1 / f_1$	damping ratio	10.0 %
$f_2 = \frac{1}{2\pi} \sqrt{\frac{k_\psi}{I}}$	natural frequency	6.8 Hz
$\xi_2 = \bar{\xi}_2 \bar{f}_2 / f_2$	damping ratio	2.4 %
Static friction - $g_0 \geq g_0^s \quad (\theta = 0)$		
$\bar{f}_1 = \frac{1}{2\pi} \sqrt{\frac{k_x + 2k_R}{m}}$	apparent frequency	6.8 Hz
$\bar{\xi}_1$	apparent damping ratio	4.7 %
$\bar{f}_2 = \frac{1}{2\pi} \sqrt{\frac{k_\psi + 2k_R l^2}{I}}$	apparent frequency	9.7 Hz
$\bar{\xi}_2$	apparent damping ratio	1.7 %

FIGURE 10: Simple 2 DOFs nonlinear model with friction used for describing the response of the two first modes (B1x and T1z). Note the presence of unrepresented angular stiffness k_ψ .

Once again, the parameters of this 2 DOFs oscillator are chosen such as to resemble the characteristics experimentally identified for RUN16. In addition to the parameters already defined for the sDOF numerical study of section 5, a unit moment of inertia I around the z axis, a unit length l and angular stiffness k_ψ are introduced. Input accelerations white noise sequences of unit variance are imposed and scaled such that $\max_t |\Gamma_x(t)| = 1$ and $\max_t |\Gamma_\psi(t)| = 0.15$ and the system (8-9) is simulated using the same previously mentioned (1/2, 1/4) Newmark scheme with $\Delta t = 0.001$ s time step. Accelerations are supposed to be measured and a 5% white noise is added to the two simulated time histories.

FIG. 11 shows the CMIF computed as dominant singular value of output PSD matrix (left) and transfer matrix (right) for varying values of g_0 ranging from asymptotic linear case $g_0 =$

0 (negligible friction forces) to $g_0 = 0.3$ (no friction). In both cases the computation of the PSD matrix involved 2000 non-overlapping 5 s-length rectangular windows. When dealing with non-linear systems, besides linear modes, stationary periodic content may appear in the output spectrum as a result of the interaction between modes (see e.g. [30] for details on NNMs and pole combination for systems with quadratic and cubic stiffness). No such pole combination is to be observed on the frequency plots, including for values $g_0 \approx 0.01 - 0.04$ where expected non-linearity is important. Friction forces only yield to a large increase of damping without changing the nicely decoupled modal nature of the dynamic response.

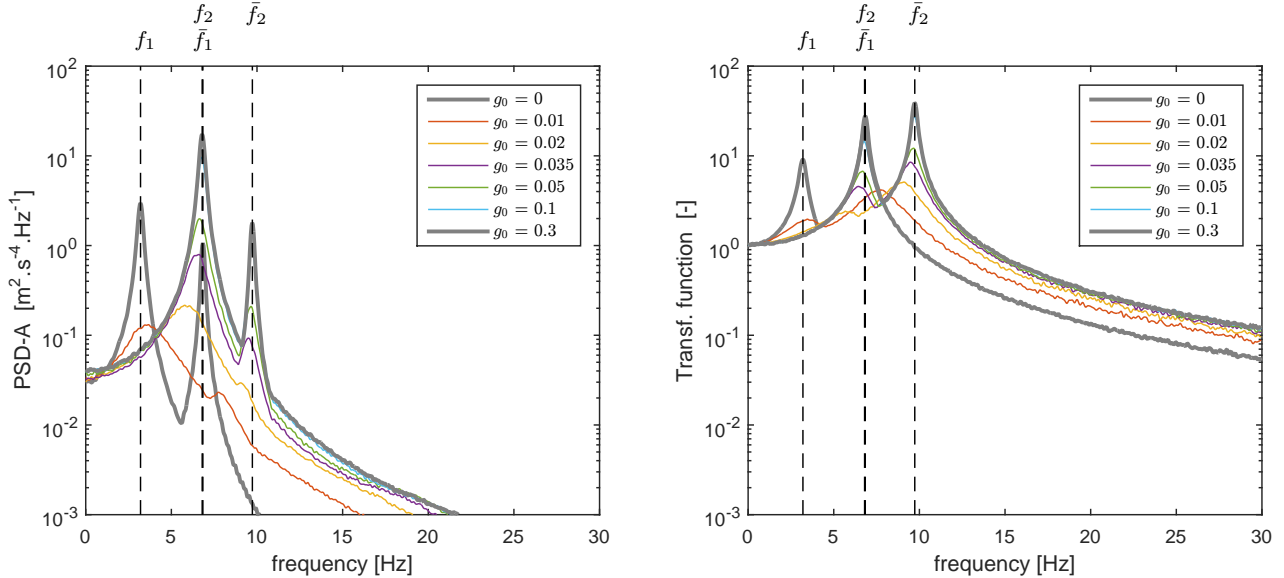


FIGURE 11: Acceleration response (CMIF) of the simple model to an adimensional biaxial white noise (Γ_x, Γ_ψ) in terms of Power Spectral Density (left) and Transfer Matrix (right) for varying friction threshold g_0 .

For assessing the performance of the subspace-based identification algorithm to capture the dominant modal response, simulations of length $T = 120$ s corresponding to varying threshold values g_0 are considered. The final identification results of the OO and IO algorithm (with the same parametrization as described in section 5) are gathered in TAB. 12. In section 5, the MPD, that was discarded from the soft validation criteria of stage (i) (see section 3) for obvious reasons when studying the single DOF toy-model, is re-introduced here, even if only two DOFs are involved. Indeed, spurious modes exhibit a default of alignment with the origin in the complex plane even if very few DOFs (even two) are observed. In every case, the automated selection algorithm [13] identified two distinct clusters of heavily populated physical candidates. As was already noticed for the single DOF toy-model of section 5, the most problematic cases correspond to values of $g_0 \in [0.01 - 0.04]$ where the proportion of nonlinear forces is important. One can note once again that a slightly better rate of identification r is obtained by the IO algorithm in the heavily nonlinear case $g_0 = 0.02$. Indeed, pole-splitting and unstabilized frequency behavior complicated the selection of the first mode in the OO case. Note that a third seemingly stable column is present in the IO case but has been discarded because of high MPD values, unstabilized damping properties and unrepresentative MTN values.

In a general manner, satisfying rates of identification r (above 70 %) have been observed when studying the 2-DOFs oscillator with Coulomb friction non-linearities using OO and IO algorithm. In each case, low MPD values have been recorded (as was also observed processing the JVP

database, see FIG. 6 and TAB. 6), making the MPD indicator a suitable soft-validation criterion when friction or elastoplastic non-linearity is involved.

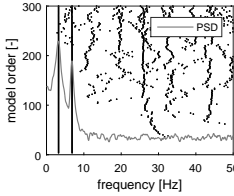
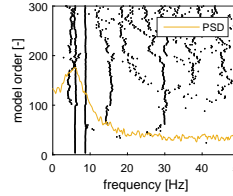
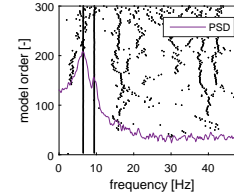
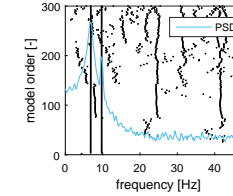
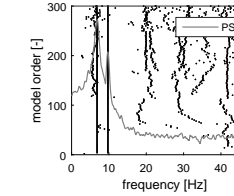
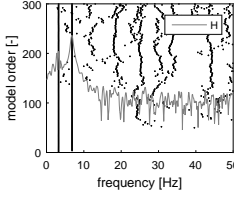
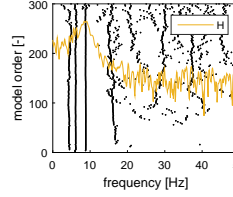
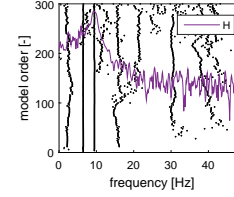
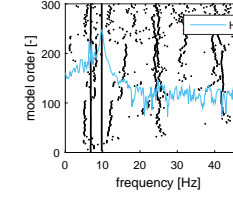
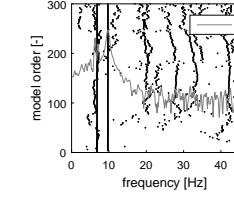
Analysis	No friction		Kinematic friction – Increased apparent damping				Static friction*				
	$g_0 = 0$		$g_0 = 0.02$	$g_0 = 0.035$	$g_0 = 0.1$	$g_0 \geq g_0^s = 0.3$					
OO											
	\bar{f} [Hz]	3.22	6.84	5.98	8.75	6.48	9.44	6.79	9.72	6.82	9.73
	$\bar{\xi}$ [%]	9.93	2.28	25.67	12.93	15.07	6.35	5.76	1.99	4.30	1.92
	MPD [rad]	0.002	0.005	0.017	0.098	0.008	0.041	0.003	0.011	0.002	0.008
	r [%]	98.7	98.7	74.0	96.0	98.7	98.7	98.7	98.7	96.0	98.7
IO											
	\bar{f} [Hz]	3.22	6.84	6.13	8.80	6.48	9.47	6.79	9.73	6.83	9.73
	$\bar{\xi}$ [%]	10.00	2.40	22.28	12.89	14.85	7.11	5.93	1.87	4.33	1.70
	MPD [rad]	0.000	0.011	0.002	0.043	0.001	0.038	0.002	0.022	0.000	0.015
	r [%]	97.3	97.3	83.3	95.3	94.0	98.0	98.7	97.3	91.3	98.7
Linearity	✓		✗		✗		✗		✓		
Targeted	\bar{f} [Hz]	3.20	6.84	–	–	–	–	–	–	6.80	9.73
	$\bar{\xi}$ [%]	10.00	2.40	–	–	–	–	–	–	4.71	1.69

TABLE 12: 2-DOFs toy-model – Subspace identification results in terms of apparent frequency and damping ratio for different friction load ratio g_0 . (*) no relative movement, $\theta = 0$.